This is to certify that the
thesis entitled
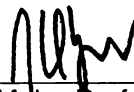
MODELING AND DESIGN OF MATERIALS FOR
CONTROLLED WAVE PROPAGAION IN PLANE GRID
STRUCTURES

presented by

LIANGKAI MA

has been accepted towards fulfillment
of the requirements for the

_____M.S._____   degree in   _MECHANICAL ENGINEERING_

_____
Major Professor's Signature

_____AUG 16, 2004_____

Date

PLACE IN RETURN BOX to remove this checkout from your record.
TO AVOID FINES return on or before date due.
MAY BE RECALLED with earlier due date if requested.

DATE DUE	DATE DUE	DATE DUE

MODELING AND DESIGN OF MATERIALS FOR CONTROLLED WAVE PROPAGTION IN PLANE GRID STRUCTURES

By

Liangkai Ma

A THESIS

Submitted to
Michigan State University
in partial fulfillment of the requirements
for the degree of

MASTER OF SCIENCE

Department of Mechanical Engineering

2004

ABSTRACT

MODELING AND DESIGN OF MATERIALS FOR CONTROLLED WAVE PROPAGTION IN PLANE GRID STRUCTURES

By

Liangkai Ma

Periodic band-gap structures prevent waves in certain frequency ranges from propagating. Materials or structures with large band gaps are desirable for many applications, including frequency filters, vibration protection devices, and wave guides. In this thesis, a simple finite element (FE) model of a periodic plane grid structure is presented. Using the Bloch-Floquet theorem and Lagrange's equations, an FE expression of an eigenvalue problem for harmonic wave propagation in an infinite periodic plane grid structure is derived. Two optimization problems are then formulated to maximize the band gap above a particular band in infinite periodic plane grid structures: one is by selective addition of non-structural masses, and the other is by a combination of selective addition of non-structural masses and adjusting of the cross section dimension (radius) of selective grid elements. Numerical implementation issues for the optimization problems are discussed and examples using symmetric periodic plane grid structures are presented. Finally, wave propagation in finite periodic plane grid structures is analyzed by considering the response of finite periodic plane grid structures subjected to harmonic loading using two applications: filter and wave guide. Special attention is paid to the response in frequency ranges of the band gaps for the corresponding infinite periodic structures.

In memory of my father

ACKNOWLEDGMENTS

TABLE OF CONTENTS

LIST OF FIGURES

LIST OF TABLES

Chapter 1   Introduction

A periodic structure consists fundamentally of a number of identical structural cells that are joined together end-to-end and/or side-by-side to form the whole structure. Examples of periodic structures include atomic lattices and similar engineering structures or materials. The atomic lattices of pure crystals constitute perfect periodic structures, which are modeled as lumped parameter systems with discrete masses (the atoms) interconnected by the inter-atomic elastic forces. In engineering structures, the mass and elasticity of structural members are continuous and constitute periodic structures when arranged in regular arrays. Periodic structures can be one dimensional (1D), two dimensional (2D) or three dimensional (3D).

Some periodic structures, such as photonic crystals, porous or fibrous materials, and structures with periodic inclusions, possess frequency band gaps that prevent waves in certain frequency ranges from propagating. The wave may be elastic, acoustic, or electromagnetic. Structures hindering elastic and acoustic waves from propagating are called phononic (acoustic) band-gap structures, and structures exhibiting stop bands for electromagnetic waves are called photonic band-gap structures. Photonic band-gap structures have great potential industrial application in optics, photonics and microwaves. Phononic band-gap structures or materials can be used to generate frequency filters, waveguides, and sound or vibration protection devices. Structures with large band gaps are desirable for such applications.

1.1 Background

Brillouin [1] gave a detailed historical review of work on wave propagation and band gaps in periodic structures from the late seventeen century to the middle of the last century. Newton initiated the study of wave propagation in periodic structures in his attempt to derive a formula for the velocity of sound. In 1881, Lord Kelvin discovered the phenomenon of cutoff frequency, the critical frequency separating stop bands and pass bands. In 1898, Vincent built the first mechanical filter model using a periodic structure made of two different masses connected to a long string through beam and spring members. In 1912, Born obtained a dispersion curve with band gaps for a 1D mass-spring model with two different masses alternating at the node points connected by the same kind of springs. From 1964 to 1995 [2], the receptance method, transfer matrix method, and finite element (FE) method were used to study wave motion in 1D, 2D and 3D continuous periodic structures such as beams, plates, and shells, etc. The natural frequencies, modes, and forced responses in periodic structures with disorders were also investigated during this period of time.

There has been an extensive search for photonic band gap materials both experimentally and theoretically since late 1980s [3]. The work on photonic band gaps has led to a revived research interest in phononic band-gap structures. Martinsson and Movchan [4] investigated the phononic band gap phenomena in infinite 2D periodic mechanical lattice structures. In their analysis, they considered a bi-atomic triangular lattice structure modeled as a truss structure and a bi-atomic square lattice structure modeled as a frame, and they found that phononic band gaps can be obtained in such structures by adjusting the lumped mass parameters at the nodes of the lattices and

stiffness parameters within the lattice structures. They also illustrated a special case in which the spectrum of the elastic lattice can be manipulated by introducing certain types of micro-structures into the elastic lattice structure.

Jensen [5] analyzed band gaps in infinite 1D and 2D mass-spring structure models and showed that for special cases analytical methods can be used to estimate the band gap bounds. In this paper, the effects of boundaries, viscous damping, and imperfections on the structural response for finite 1D and 2D periodic structures subjected to periodic loading in frequency gap ranges of corresponding infinite periodic structures were also investigated.

Topology optimization techniques have been used to optimize phononic band gaps in elastic materials by Sigmund and Jensen [6-8]. Their results showed that periodic structures made of a mixture of materials of high contrast properties such as density and Young's modulus tend to exhibit band gaps. A projected gradient ascent optimization method and an optimization-based evolution algorithm for producing band gaps in 2D photonic crystals have been presented by Cox and Dobson [9, 10]. According to their research, larger photonic gaps can be obtained by increasing material contrast.

Elastic wave propagation in various structures has also been investigated by other authors, including Parmley *et al.* [11] (mass chains), Kafesaki *et al.* [12] and Vasseur *et al.* [13] (composites), and Sigalas and Economou [14] (plates). In early work, Heckel [15] presented a theoretical analysis of vibration in periodic plane grids made of crossed-beams. By assuming that the distance between adjacent intersections is longer than the wave length, Heckel found that that there are bands of high attenuation and bands of no attenuation for bending-wave transmission through plane grids.

In this work, the wave propagation in plane grids is investigated using a finite element model. The analysis of plane wave propagation in periodic structures using FE methods has been discussed by Orris and Petyt [16] and Langlet *et al.* [17]. Orris and Petyt presented a method for using FE technique to evaluate the phase constant, which is associated with the normal modes and natural frequencies of a periodic structure. Using this method they studied wave propagation in a periodically supported infinite beam and a skin-rib structure. Langlet *et al.* applied FE approach to the investigation of plane acoustic wave propagation in periodic materials containing inclusions or cylindrical pores.

1.2 Research objective

No band gaps exist in infinite homogeneous periodic structures or materials, and thus the following question rises naturally: Which periodic structures produce the largest band gaps? The aim of this work is to answer this question by means of optimization problem formulations for plane grid structures using an FE model. The optimization problem is to maximize the band gap above a particular frequency band by selective addition of non-structural masses and by a combination of selective addition of non-structural masses and adjusting of the cross section dimension (radius) of selective grid elements. The problem can be divided into the following sub-problems:

1. Build an FE model for plane grid structures.

2. Apply Bloch-Floquet theorem and derive an eigenvalue problem that can be used to compute all natural frequencies for infinite periodic plane grid structures.

3. Formulate optimization problems to facilitate numerical implementation of maximizing band gaps in infinite periodic plane grid structures.

4. Obtain the optimal design by numerical implementation of the optimization problems.

5. Verify the optimal design.

1.3 Approach

An infinite 2D periodic grid structure may be split into successive irreducible cells. The infinite periodic structure can be characterized by its representative cell using Bloch-Floquet theorem [1, 19], and an FE expression of the eigenvalue problem for infinite periodic plane grid structures can be derived by analyzing this representative cell. The eigenfrequencies for current design are obtained by solving this eigenvalue problem. The gap size for current design is evaluated using these computed eigenfrequencies and the gradients of the band gap size with respect to design variables are computed using the eigenvectors associated with the critical eigenvalues determining the current band gap size. The optimization problems are then formulated to solve for the optimal design. Finally, finite periodic structures are constructed using the obtained optimal design to verify the presence of band gaps in the structures.

1.4 Organization

The remainder of the thesis is presented as follows:

Chapter 2 describes an infinite 2D periodic structure and introduces the concept of representative cell and the Bloch-Floquet theorem.

Chapter 3 defines an FE model for 2D grid with out-of-plane vibration (wave propagation) and presents a complete derivation of FE expression of the eignenvalue problem for infinite 2D periodic grid structures.

Chapter 4 discusses formulations of the optimization problems for infinite 2D periodic grid structures and numerical implementation issues.

Chapter 5 presents the examples and discusses the optimal results.

Chapter 6 analyzes the response of finite periodic grid structures using two applications of band-gap structures: as a filter and as a wave guide.

Chapter 7 summarizes the research and predicts possible opportunities for future work.

.

Chapter 2   Infinite 2D Periodic Structure

In this chapter, an infinite 2D periodic structure is described and the concept of representative cell and the Bloch-Floquet theorem are introduced. An infinite 2D periodic structure is characterized by its representative cell, and the wave propagation in infinite periodic structures is governed by the Bloch-Floquet theorem.

2.1   Representative Cell

A 2D periodic structure, Ω^P, is a plane structure that can be constructed by periodically repeating a sub-section, Ω, of the structure through translations along the two vectors, $\mathbf{t}^{(1)}$ and $\mathbf{t}^{(2)}$, called the tiling vectors or translation vectors, i.e.,

$$\Omega^P = \bigcup_{\mathbf{n} \in Z^2} (\Omega + \mathbf{Tn})$$

where $\mathbf{T} = [\mathbf{t}^{(1)}, \mathbf{t}^{(2)}]$, $\mathbf{n} = (n_1, n_2)^T$. A pictorial example of these terms is shown in Figure 1. The integer numbers n_1 and n_2 represent cell translations along $\mathbf{t}^{(1)}$ and $\mathbf{t}^{(2)}$, respectively. Ω is called the representative cell of the 2D periodic structure. An irreducible cell is the smallest representative cell capable of filling Ω^P through a process of translations along the two tiling vectors. In this work, we only consider cells that can be fully circumscribed by the parallelepiped spanned by the tiling vectors. Let cell number $\mathbf{n} = (n_1, n_2)^T$ denote an arbitrary cell $\Omega^{(\mathbf{n})} = \Omega + \mathbf{Tn}$. For the representative cell Ω, $\mathbf{n} = (0,0)^T$. To facilitate analysis, additional nodes, denoted by the void dots (Figure 2), are added to the representative cell to provide each element in the cell, denoted by lines between dots, with two nodes. To distinguish the original nodes (denoted by solid

dots) from the added nodes (denoted by void dots), we call the former master nodes and the later slave nodes of the representative cell. Let NMN and NSN denote respectively the total number of master nodes and slave nodes in the representative cell. A master node in an arbitrary cell $\Omega^{(\mathbf{n})}$ can be identified by cell number $\mathbf{n}$ and a node index j. A master node in cell $\mathbf{n}$ is a member of the set $\{(\mathbf{n}, j)\}_{j=1}^{NMN}$. Let $(\mathbf{0}, j)$ be a master node in the representative cell Ω, where $j \in \{1, 2, ... NMN\}$. Then the master node $(\mathbf{n}, j)$ in $\Omega^{(\mathbf{n})}$ is an image of master node j in Ω.

(a) The whole structure

(b) Irreducible cell

(c) Tiling vectors
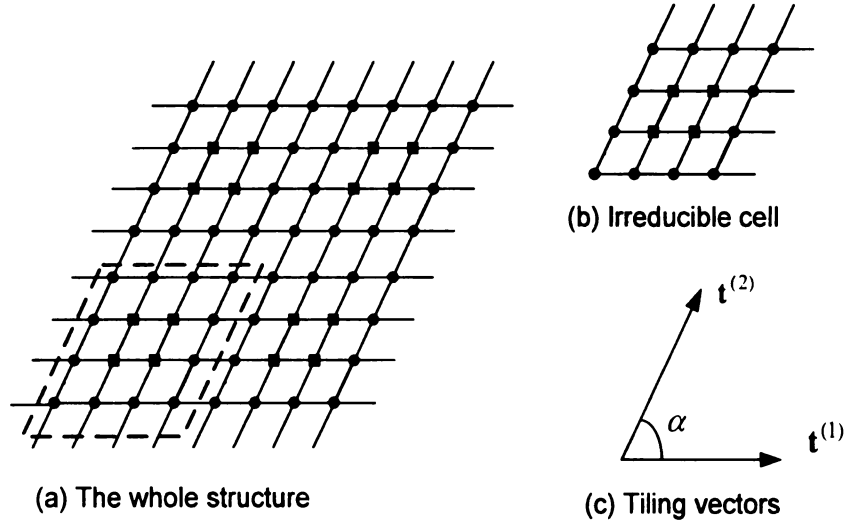
Figure 1. Infinite 2D periodic structure
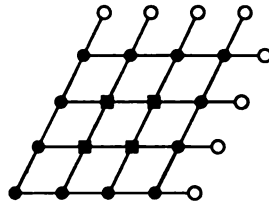
Figure 2. Representative cell Ω with added slave nodes

2.2 Bloch-Floquet Theorem

An important theorem, known as Bloch-Floquet theorem [1, 18], states that the wave propagation through a periodic lattice has the form

$$\psi = A_{(\hat{\mathbf{k}})} e^{i\hat{\mathbf{k}}\mathbf{T}\mathbf{n}} \tag{1}$$

where ψ is a property associated with a node point of the lattice such as the displacement of a node, A is a function, generally depending on the wave vector $\hat{\mathbf{k}} = (\hat{k}_1, \hat{k}_2)$, which is periodic with period associated with the lattice periodicity. More on the meaning of $\hat{\mathbf{k}}$ will appear later in Section 3.6.

Let $\mathbf{u}^{(\mathbf{0},j)}$ denote the generalized displacements of master node $(\mathbf{0}, j)$ in Ω. Applying Bloch-Floquet theorem (1), the generalized displacements of master node $(\mathbf{n}, j)$ in $\Omega^{(\mathbf{n})}$ can be expressed as

$$\mathbf{u}^{(\mathbf{n},j)} = e^{i\hat{\mathbf{k}}\mathbf{T}\mathbf{n}} \mathbf{u}^{(\mathbf{0},j)} \tag{2}$$

If we set

$$k_1 = (\hat{\mathbf{k}} \cdot \mathbf{t}^{(1)}) \text{ and } k_2 = (\hat{\mathbf{k}} \cdot \mathbf{t}^{(2)}) \tag{3}$$

then the above equation can be expressed as

$$\mathbf{u}^{(\mathbf{n},j)} = e^{i\mathbf{k}\cdot\mathbf{n}} \mathbf{u}^{(\mathbf{0},j)} = e^{i(n_1 k_1 + n_2 k_2)} \mathbf{u}^{(\mathbf{0},j)} \tag{4}$$

where $\mathbf{k} = (k_1, k_2)$ and the real parameters k_1, k_2 represent the changes in phase of a wave between a cell and its immediate neighbor cells along tiling vectors $\mathbf{t}^{(1)}$ and $\mathbf{t}^{(2)}$ respectively.

Let $\mathbf{u}^m \in C^{NDM}$ and $\mathbf{u}^s \in C^{NDS}$ be the displacement vectors of master nodes and slave nodes of the representative cell. Here NDM denotes the number of degrees of

freedom associated with master nodes, and *NDS* denotes the number of degrees of freedom associated with slave nodes in the cell. Since slave nodes in the representative cell are master nodes in the neighbor cells of the representative cell, applying (2) to all slave nodes in the representative cell permits $\mathbf{u}^s$ to be expressed in terms of $\mathbf{u}^m$ as

$$\mathbf{u}^s = \mathbf{B}(\mathbf{k})\mathbf{u}^m \tag{5}$$

where $\mathbf{B} \in C(NDS, NDM)$. $\mathbf{B}$ is called here the representative cell's quasi-periodicity matrix and it depends on the vector $\mathbf{k}$.

Chapter 3   FE Expression of Eigenvalue Problem for Infinite 2D Grids

3.1   Introduction to the FE model

Plane grid structures are typically made of a series of intersecting long, rigid linear

elements such as beams or trusses. In this work, only plane grids made of crossed-beams

with circular cross sections are considered. Joints at points of intersection are assumed

rigid so that a state of deflection compatibility exists at each point of intersection. In the

FE model used here, one beam element is used to model each grid element i.e. only one

element is used to model the segment between two adjacent intersections of a grid

structure.

3.2   2D Grid Element Stiffness and Mass Matrices

A 2D grid element consists of two nodes and each node has three degrees of freedom:

a vertical deflection along the z axis d_{iz} (normal to the plane of grid), a torsional rotation

φ_{ix} about the x axis (the longitudinal axis of element), and a bending rotation φ_{iy} about

the y axis to account for out-of-plane bending (Figure 3), where i is the node index and

$i=1,2$.
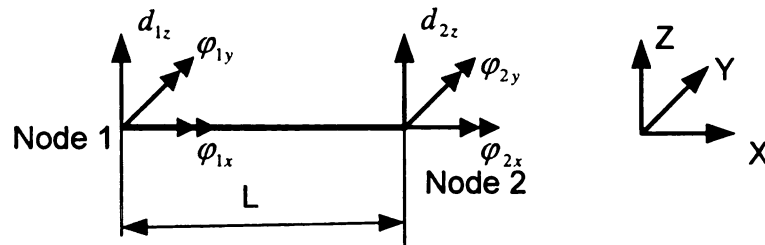
Figure 3. 2D Grid element and its nodal degrees of freedom

Assuming cubic displacement shape functions for bending and linear displacement shape functions for torsion within each element, the grid element stiffness and lumped mass matrices at the local coordinates are given by

$$\hat{S}^e = \begin{bmatrix} \dfrac{12EI}{L^3} & 0 & \dfrac{6EI}{L^2} & \dfrac{-12EI}{L^3} & 0 & \dfrac{6EI}{L^2} \\[2mm] & \dfrac{GJ}{L} & 0 & 0 & \dfrac{-GJ}{L} & 0 \\[2mm] & & \dfrac{4EI}{L} & \dfrac{-6EI}{L^2} & 0 & \dfrac{2EI}{L} \\[2mm] & & & \dfrac{12EI}{L^3} & 0 & \dfrac{-6EI}{L^2} \\[2mm] & & & & \dfrac{GJ}{L} & 0 \\[2mm] \text{Symmetry} & & & & & \dfrac{4EI}{L} \end{bmatrix} \tag{6}$$

$$\hat{M}^e = \begin{bmatrix} \dfrac{\rho AL}{2} & 0 & 0 & 0 & 0 & 0 \\[2mm] 0 & \dfrac{\rho JL}{2} & 0 & 0 & 0 & 0 \\[2mm] 0 & 0 & \dfrac{\rho AL^3}{24} & 0 & 0 & 0 \\[2mm] 0 & 0 & 0 & \dfrac{\rho AL}{2} & 0 & 0 \\[2mm] 0 & 0 & 0 & 0 & \dfrac{\rho JL}{2} & 0 \\[2mm] 0 & 0 & 0 & 0 & 0 & \dfrac{\rho AL^3}{24} \end{bmatrix} \tag{7}$$

where E is the material Young's modulus, G is the material shear modulus, ρ is the material density, I is the second moment of area of the cross section, A is the area of the cross section along the x axis, J is the torsional constant about the x axis, L is the length of the grid element, and the degrees of freedom are, in order, 1) vertical deflection along the z axis, 2) torsional rotation about the x axis, 3) bending rotation about the y axis.

The transformation matrix relating local to global degrees of freedom for a grid element is

$$L = \begin{bmatrix} 1 & 0 & 0 & 0 & 0 & 0 \\ 0 & \cos\theta & \sin\theta & 0 & 0 & 0 \\ 0 & -\sin\theta & \cos\theta & 0 & 0 & 0 \\ 0 & 0 & 0 & 1 & 0 & 0 \\ 0 & 0 & 0 & 0 & \cos\theta & \sin\theta \\ 0 & 0 & 0 & 0 & -\sin\theta & \cos\theta \end{bmatrix} \tag{8}$$

where θ is the rotation angle taken counterclockwise from the global positive coordinate system to the local positive coordinate system in the x-y plane about z axis. The global stiffness and mass matrices for a given grid element arbitrarily oriented in the x-y plane are

$$S^e = L^T \hat{S}^e L \tag{9}$$

$$M^e = L^T \hat{M}^e L \tag{10}$$

3.3 Stiffness and Mass Matrices for a 2D Grid Representative Cell

Following a standard FE assembly procedure, the stiffness and mass matrices for a 2D grid representative cell S^{cell} and M^{cell} can be constructed and expressed in partitioned form as follows:

$$S^{cell} = \begin{bmatrix} S^{mm} & S^{ms} \\ S^{sm} & S^{ss} \end{bmatrix} \tag{11}$$

$$M^{cell} = \begin{bmatrix} M^{mm} & M^{ms} \\ M^{sm} & M^{ss} \end{bmatrix} \tag{12}$$

These matrices are of dimension $(NDM+NDS)$ x $(NDM+NDS)$ and they have the following properties:

1. S^{cell} and M^{cell} are real and symmetric.

- 13 -

2. $\mathbf{S}^{ss}$ and $\mathbf{M}^{ss}$ are block diagonal with symmetric sub-matrices of order *NDN* x

NDN, where *NDN* denotes the number of degrees of freedom per node. In 2D grids,

NDN=3. This property follows from the fact that there is no element connection between

any two slave nodes in the representative cell, by the definition of the representative cell.

Using (5), the stiffness and mass matrices $\mathbf{S}^{cell}$ and $\mathbf{M}^{cell}$ can be reduced so that the

resulting equations of motion are linearly independent and expressed only in terms of the

master degrees of freedom. This is described in detail in the following section.

3.4 Derivation of Equations of Motion

Let $\mathbf{u}^{cell} = [\mathbf{u}^m, \mathbf{u}^s]^T$ be the displacement vector of all nodes in a representative cell.

Then the kinetic energy (*T*) and potential energy (*V*) of the representative cell can be

expressed as

$$T = \frac{1}{2}(\dot{\mathbf{u}}^{cell})^* \mathbf{M}^{cell} \dot{\mathbf{u}}^{cell} \qquad (13)$$

$$V = \frac{1}{2}(\mathbf{u}^{cell})^* \mathbf{S}^{cell} \mathbf{u}^{cell} \qquad (14)$$

Here $()^*$ denotes Hermitian transpose. Let $\mathbf{f}^m$ and $\mathbf{f}^s$ be the force vectors applied,

respectively, at the master nodes and slave nodes in the representative cell, and let

$\mathbf{f}^{cell} = [\mathbf{f}^m, \mathbf{f}^s]^T$. The virtual work δW of the external force $\mathbf{f}^{cell}$ through a virtual

displacement $\delta\mathbf{u}^{cell}$ can be expressed as

$$\delta W = (\delta\mathbf{u}^{cell})^* \mathbf{f}^{cell} \qquad (15)$$

where $\delta\mathbf{u}^{cell} = [\delta\mathbf{u}^m, \delta\mathbf{u}^s]^T$.

Define a mass matrix $\mathbf{M}$, stiffness matrix $\mathbf{K}$ and force vector $\mathbf{f}$, so that

$$T = \frac{1}{2}(\dot{\mathbf{u}}^m)^* \mathbf{M} \dot{\mathbf{u}}^m \tag{16}$$

$$V = \frac{1}{2}(\mathbf{u}^m)^* \mathbf{K} \mathbf{u}^m \tag{17}$$

and

$$\delta W = (\delta \mathbf{u}^m)^* \mathbf{f} \tag{18}$$

Using (12), equation (13) can be written in matrix form as

$$T = \frac{1}{2}[(\dot{\mathbf{u}}^m)^*, (\dot{\mathbf{u}}^s)^*] \begin{bmatrix} \mathbf{M}^{mm} & \mathbf{M}^{ms} \\ \mathbf{M}^{sm} & \mathbf{M}^{ss} \end{bmatrix} \begin{bmatrix} \dot{\mathbf{u}}^m \\ \dot{\mathbf{u}}^s \end{bmatrix}$$

Upon substitution of (5) and noting that $\mathbf{B}$ is not a function of time, the above equation yields

$$T = \frac{1}{2}[(\dot{\mathbf{u}}^m)^*, (\mathbf{B}\dot{\mathbf{u}}^m)^*] \begin{bmatrix} \mathbf{M}^{mm} & \mathbf{M}^{ms} \\ \mathbf{M}^{sm} & \mathbf{M}^{ss} \end{bmatrix} \begin{bmatrix} \dot{\mathbf{u}}^m \\ \mathbf{B}\dot{\mathbf{u}}^m \end{bmatrix}$$

$$= \frac{1}{2}(\dot{\mathbf{u}}^m)^* (\mathbf{M}^{mm} + \mathbf{B}^* \mathbf{M}^{sm} + \mathbf{M}^{ms}\mathbf{B} + \mathbf{B}^* \mathbf{M}^{ss}\mathbf{B})\dot{\mathbf{u}}^m$$

Comparing the above equation with (16), we conclude that

$$\mathbf{M} = \mathbf{M}^{mm} + \mathbf{B}^* \mathbf{M}^{sm} + \mathbf{M}^{ms}\mathbf{B} + \mathbf{B}^* \mathbf{M}^{ss}\mathbf{B} \tag{19}$$

Similarly, from (11), (14) and (17), the stiffness matrix $\mathbf{K}$ can be shown to have the form

$$\mathbf{K} = \mathbf{S}^{mm} + \mathbf{B}^* \mathbf{S}^{sm} + \mathbf{S}^{ms}\mathbf{B} + \mathbf{B}^* \mathbf{S}^{ss}\mathbf{B} \tag{20}$$

Finally, (15) can be written in matrix form as

$$\delta W = [\delta \mathbf{u}^m, \delta \mathbf{u}^s]^* \begin{bmatrix} \mathbf{f}^m \\ \mathbf{f}^s \end{bmatrix} = [(\delta \mathbf{u}^m)^*, (\mathbf{B}\delta \mathbf{u}^m)^*] \begin{bmatrix} \mathbf{f}^m \\ \mathbf{f}^s \end{bmatrix}$$

$$= (\delta \mathbf{u}^m)^* (\mathbf{f}^m + \mathbf{B}^* \mathbf{f}^s).$$

Comparing the above equation with (18), we conclude that

$$\mathbf{f} = (\mathbf{f}^m + \mathbf{B}^* \mathbf{f}^s) \tag{21}$$

Choose $\mathbf{u}^m \in C^{NDM}$ as generalized coordinates so that Lagrange's equations take the form

$$\frac{d}{dt}(\frac{\partial L}{\partial (\dot{\mathbf{u}}^m)}) - \frac{\partial L}{\partial (\mathbf{u}^m)} = \mathbf{f} \tag{22}$$

where the Lagrangian

$$L = T - V \tag{23}$$

and the reduced generalized force vector $\mathbf{f}$ is given by (21).

Substituting (16) and (17) into (22) and (23), we obtain the equations of motion:

$$\mathbf{M}\ddot{\mathbf{u}}^m + \mathbf{K}\mathbf{u}^m = \mathbf{f} \tag{24}$$

where $\mathbf{M}$ and $\mathbf{K}$ are the reduced mass and stiffness matrices.

3.5   Derivation of Eigenvalue Problem

Assuming a time-harmonic form of wave propagation in the periodic structure, let

$$\mathbf{u}^m = \mathbf{a}e^{i\omega t} \tag{25}$$

where $\mathbf{a}$ is the wave amplitude vector, ω is the wave vibration frequency and $i = \sqrt{-1}$. Let $\mathbf{f}=0$ and introduce (25) into (24). It follows that

$$(\mathbf{K} - \lambda \mathbf{M})\mathbf{a} = 0 \tag{26}$$

where $\lambda = \omega^2$ is an eigenvalue, $\mathbf{a}$ is the eigenvector corresponding to λ, $\mathbf{M}$ and $\mathbf{K}$ are given by (19) and (20) and they are functions of $\mathbf{k} = (k_1, k_2)$. Equation (26) should be

solved for $\mathbf{k} \in \Re^2$, but all eigenfrequencies can be obtained by solving (26) using $\mathbf{k} \in [-\pi,\pi]^2$ because of structure periodicity. This is shown next.

3.6 Irreducible 2D Brillouin Zone for Symmetric Structures

In (4), k_1 and k_2 can be replaced by k_1' and k_2' without changing the relationship between $\mathbf{u}^{(\mathbf{n},j)}$ and $\mathbf{u}^{(0,j)}$, letting

$$k_i' = k_i + 2\pi n_i \tag{27}$$

where m_i are integers and i=1, 2. It follows from (5), (19) and (20) that $\mathbf{M}$ and $\mathbf{K}$ remain unchanged when k_i is replaced by k_i'. Combining with (26), we conclude that the eigenfrequencies of a 2D periodic structure are 2π periodic in k_1,k_2. Thus all eigenfrequencies can be obtained by solving (26) using $\mathbf{k} \in [-\pi,\pi]^2$, which is equivalent to the first 2D Brillouin zone [1] in the reciprocal lattice defined next.

The direct lattice described by the tiling vectors $\mathbf{t}^{(1)}$ and $\mathbf{t}^{(2)}$ is the set

$$\mathbf{H} = \{\mathbf{y} \in \Re^2 : \mathbf{y} = n_1\mathbf{t}^{(1)} + n_2\mathbf{t}^{(2)}, n_1, n_2 \in Z\}$$

For each direct lattice, a reciprocal lattice can be constructed using basis vectors $\mathbf{d}^{(1)}$ and $\mathbf{d}^{(2)}$ given by the equations

$$\mathbf{t}^{(i)} \cdot \mathbf{d}^{(j)} = 2\pi\delta_{ij}, \quad i,j=1, 2 \tag{28}$$

In the reciprocal lattice, the value of $\hat{\mathbf{k}}'$ corresponding to the values of k_1' and k_2' in (27) can be found to be

$$\hat{\mathbf{k}}' = \hat{\mathbf{k}} + m_1\mathbf{d}^{(1)} + m_2\mathbf{d}^{(2)} \tag{29}$$

This can be shown using (3) and (28) as follows:

$$k_1' = (\hat{\mathbf{k}}' \cdot \mathbf{t}^{(1)})$$

$$= (\hat{\mathbf{k}} \cdot \mathbf{t}^{(1)}) + m_1 (\mathbf{d}^{(1)} \cdot \mathbf{t}^{(1)}) + m_2 (\mathbf{d}^{(2)} \cdot \mathbf{t}^{(1)})$$

$$= k_1 + 2\pi m_1$$

Similarly, $k_2' = k_2 + 2\pi m_2$

The above discussion shows that the eigenfrequency of a 2D periodic structure is a periodic function of wave vector $\hat{\mathbf{k}}$ in the reciprocal lattice with basis vectors $\mathbf{d}^{(1)}$ and $\mathbf{d}^{(2)}$. Because of this periodicity, all eigenfrequencies can be obtained by solving (26) using the first 2D Brillouin zone in reciprocal lattice, $\hat{\mathbf{k}} \in \frac{1}{2}[-\mathbf{d}^{(i)}, \mathbf{d}^{(i)}], i = 1,2$. For symmetric periodic structures, the first 2D Brillouin zone can be reduced further.

Define unit vectors $\hat{\mathbf{t}}^{(1)}$ and $\hat{\mathbf{t}}^{(2)}$ of a direct lattice and unit vectors $\hat{\mathbf{d}}^{(1)}$ and $\hat{\mathbf{d}}^{(2)}$ of its corresponding reciprocal lattice so that

$$\hat{\mathbf{t}}^{(i)} = \frac{\mathbf{t}^{(i)}}{\left\| \mathbf{t}^{(i)} \right\|}, i=1,2$$

$$\hat{\mathbf{d}}^{(i)} = \frac{\mathbf{d}^{(i)}}{\left\| \mathbf{d}^{(i)} \right\|}, i=1,2$$

where $\| \ \|$ denotes the length of a vector.

Let the geometric center of the representative cell be the origin. Then any point $\mathbf{h}$ in the representative cell is of the form

$$\mathbf{h} = h_1 \mathbf{t}^{(1)} + h_2 \mathbf{t}^{(2)} = h_1 \left\| \mathbf{t}^{(1)} \right\| \hat{\mathbf{t}}^{(1)} + h_2 \left\| \mathbf{t}^{(2)} \right\| \hat{\mathbf{t}}^{(2)} = \xi_1 \hat{\mathbf{t}}^{(1)} + \xi_2 \hat{\mathbf{t}}^{(2)}$$

- 18 -

where $\xi_i = h_i \left\| \mathbf{t}^{(i)} \right\|$ and $h_i \in [-\frac{1}{2}, \frac{1}{2})$, i=1, 2.

Similarly, any point $\hat{\mathbf{k}}$ in the first Brillouin zone can be expressed by a vector

$$\hat{\mathbf{k}} = \eta_1 \mathbf{d}^{(1)} + \eta_2 \mathbf{d}^{(2)} = \eta_1 \left\| \mathbf{d}^{(1)} \right\| \hat{\mathbf{d}}^{(1)} + \eta_2 \left\| \mathbf{d}^{(2)} \right\| \hat{\mathbf{d}}^{(2)} = \hat{k}_1 \hat{\mathbf{d}}^{(1)} + \hat{k}_2 \hat{\mathbf{d}}^{(2)}$$

where $\hat{k}_i = \eta_i \left\| \mathbf{d}^{(i)} \right\|$ and $\eta_i \in [-\frac{1}{2}, \frac{1}{2}]$, i=1, 2.

Let $\mathbf{x}$ represent the material parameters (e.g. density, Young's modulus, shear modulus, cross section area, length of element, nonstructural mass at nodes etc.) that affect matrices $\mathbf{S}^{cell}$ or $\mathbf{M}^{cell}$ in (11) and (12). If $\mathbf{x}$ remains unchanged in the direct lattice under the transformations

$$(\xi_1, \xi_2) \mapsto (-\xi_1, \xi_2), \ (\xi_1, \xi_2) \mapsto (\xi_1, -\xi_2), \ (\xi_1, \xi_2) \mapsto (\xi_2, \xi_1) \tag{30}$$

for $\xi_i \in \frac{1}{2}(-\left\| \mathbf{t}^{(i)} \right\|, \left\| \mathbf{t}^{(i)} \right\|)$, i=1,2, then eigenfrequencies of (26) remain unchanged in reciprocal lattice under the following transformations

$$(\hat{k}_1, \hat{k}_2) \mapsto (-\hat{k}_1, \hat{k}_2), \ (\hat{k}_1, \hat{k}_2) \mapsto (\hat{k}_1, -\hat{k}_2), \ (\hat{k}_1, \hat{k}_2) \mapsto (\hat{k}_2, \hat{k}_1)$$

Accordingly, the first 2D Brillouin zone $[-\pi, \pi]^2$ in $\mathbf{k}$ space can be further reduced to the triangle zone enclosed by Ψ=[A-B-C-A] in Figure 4 (see [9]). Many authors [4-10] use only the boundary Ψ=[A-B-C-A] of the triangle for computation purposes. In this work, we consider only optimal solutions with symmetry defined by (30), and the boundary of the triangle is used for numerical implementation.

3.7 Dispersion Diagram

For a 2D grid, the Hermitian mass matrix **M** is positive definite and the Hermitian stiffness matrix **K** is positive semi-definite. It follows that the solution to (26) with **k**
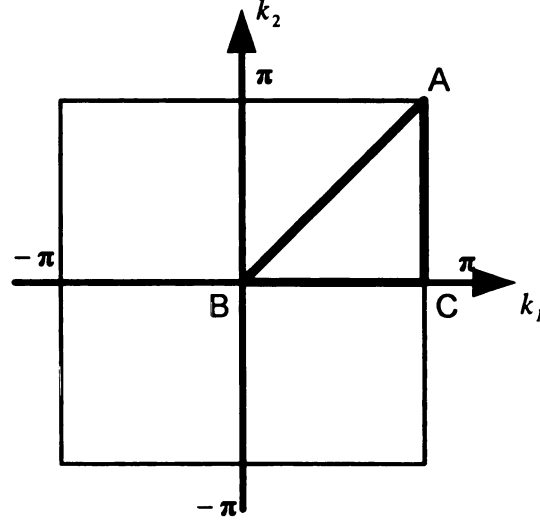

Figure 4. Irreducible 2D Brillouin zone for symmetric structures

ranging over Ψ is composed of a discrete sequence of real, nonnegative eigenvalues. If the eigenvalues of (26) are plotted against $\mathbf{k} \in \Psi$, the resulting diagram is called dispersion diagram or Bloch spectrum (see Figure 5). Obviously, each eigenvalue λ and the Bloch spectrum of (26) depend on the mass and stiffness of the structure. For a fixed **k,** we enumerate the eigenvalue bands as $0 \leq \lambda_1(\mathbf{x},\mathbf{k}) \leq \lambda_2(\mathbf{x},\mathbf{k}) \leq \lambda_3(\mathbf{x},\mathbf{k}) \leq \cdots$ (recall that **x** denotes the material or structure parameters). For a given material or structure, the eigenvalue bands are fixed and we express them as

$$\Pi = \{\lambda_j(\mathbf{k}) : \mathbf{k} \in \Psi, j = 1,2,3\cdots\}$$

Waves of frequency ω such that $\omega^2 \notin \Pi$ do not propagate in the structure. If there exists a frequency ω_0 which satisfies

$$\lambda_j(\mathbf{k}) < \omega_0^2 < \lambda_{j+1}(\mathbf{k}) \text{ for any } \mathbf{k} \in \Psi$$

we say that there is a band gap between eigenvalue bands j and $j+1$, and the band gap G is determined by the minimum of band $j+1$ and the maximum of band j, i.e.
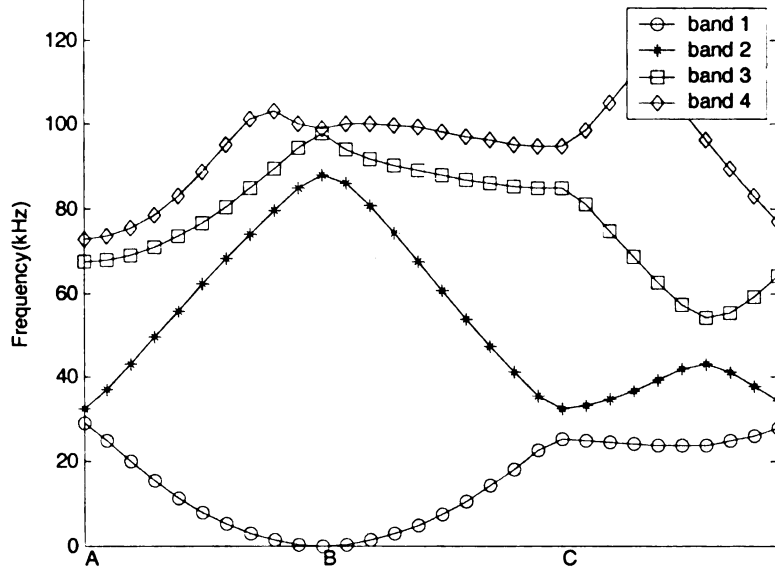

Figure 5. A typical dispersion diagram showing the lowest four bands

$$G = \min_{\mathbf{k} \in \Psi} \lambda_{j+1}(\mathbf{k}) - \max_{\mathbf{k} \in \Psi} \lambda_j(\mathbf{k}) \tag{31}$$

Clearly, the solutions $\mathbf{k}^*$ to the minimum and maximum problems in (31) are important information for determining the band gaps in a periodic structure. Assuming that the eigenvalues at A, B, and C (the vertices of the triangle in Figure 4) are distinct, one can show that A, B, and C are stationary points on the dispersion diagram and therefore potential candidate solutions $\mathbf{k}^*$. A complete proof is given next.

3.7.1 Stationary Points on the Dispersion Diagram

Proposition 1. For a representative cell of a 2D periodic lattice structure, let

$\mathbf{B} \in C(NDS, NDM)$ be its quasi-periodicity matrix. Then for any matrix

$\mathbf{W} \in \Re(NDS, NDS)$ that is block diagonal with symmetric sub-matrices of order NDN x NDN and independent of wave vector $\mathbf{k}$, $\mathbf{B}^*\mathbf{W}\mathbf{B}$ is symmetric and independent of $\mathbf{k}$.

Proof:

We divide the NDS rows and NDM columns of $\mathbf{B}$ into NSN row groups and NMN column groups so that $\mathbf{B}$ is partitioned to include NSN x NMN sub-matrices and each sub-matrix is of order NDN x NDN. Let β ($\beta \in \{1,2,...NSN\}$) denote an arbitrary slave node in a representative cell, $\mathbf{n}_\beta$ denote the cell number for the cell in which node β is a master node, j ($j \in \{1,2,...NMN\}$) denote an arbitrary master node in the representative cell, and $\mathbf{Y}^j$ denote the set of slave nodes in the representative cell that have the same master node index j in the neighbor cells of the representative cell, i.e.

$$\mathbf{Y}^j = \{\beta : (\mathbf{n}_\beta, j) \in \Omega^{(\mathbf{n}_\beta)} \text{ is an image of node } (0, j) \in \Omega \}$$

By definition of quasi-periodicity matrix $\mathbf{B}$ (5), the sub-matrix $\mathbf{B}_{\beta j}$, which is located at the βth row group and jth column group, relates the displacements of slave node β ($\mathbf{u}^\beta$) and the displacements of master node j ($\mathbf{u}^j$) through

$$\mathbf{u}^\beta = \mathbf{u}^{(\mathbf{n}_\beta, j)} = \mathbf{B}_{\beta j}\mathbf{u}^{(0, j)} = \mathbf{B}_{\beta j}\mathbf{u}^j \tag{32}$$

The entries of $\mathbf{B}_{\beta j}$ are given by

$$\mathbf{B}_{\beta j} = \begin{cases} e^{i\mathbf{k}\bullet\mathbf{n}_\beta}\mathbf{I}, & \beta \in \mathbf{Y}^j \\ 0 & \beta \notin \mathbf{Y}^j \end{cases} \tag{33}$$

where $\mathbf{I}$ is an identity matrix and 0 is a zero matrix of order NDN x NDN.

Since matrix $\mathbf{W} \in \Re(NDS, NDS)$ is block diagonal with sub-matrices of order NDN x NDN, it follows that

- 22 -

$$(\mathbf{B}^*\mathbf{WB})_{mn} = \sum_{\alpha=1}^{NSN} \sum_{\beta=1}^{NSN} (\mathbf{B}^*)_{m\alpha} \mathbf{W}_{\alpha\beta} \mathbf{B}_{\beta n} = \sum_{\alpha=1}^{NSN} \sum_{\beta=\alpha} (\mathbf{B}^*)_{m\alpha} \mathbf{W}_{\alpha\beta} \mathbf{B}_{\beta n}$$

$m, n = 1, 2, \ldots NMN.$ (34)

Applying (33) and the identity $\overline{e^{i\gamma}} = e^{-i\gamma}$, we have

$$(\mathbf{B}^*)_{m\alpha} = \overline{\mathbf{B}}_{\alpha m} = \begin{cases} e^{-i\mathbf{k}\bullet\mathbf{n}\alpha}\mathbf{I}, & \alpha \in Y^m \\ 0 & \alpha \notin Y^m \end{cases}$$ (35)

and

$$\mathbf{B}_{\beta n} = \begin{cases} e^{i\mathbf{k}\bullet\mathbf{n}\beta}\mathbf{I}, & \beta \in Y^n \\ 0 & \beta \notin Y^n \end{cases}$$ (36)

By definition, a slave node can be an image of only one master node in the representative cell, i.e.

$$Y^m \bigcap Y^n = \phi, \; m \neq n, \; m,n \in \{1,2,\ldots NMN\}$$ (37)

Combining with (33), (37) simply says that the βth ($\beta \in \{1,2,\ldots NSN\}$) row group of $\mathbf{B}$ has only one nonzero entry, while the jth ($j \in \{1,2,\ldots NMN\}$) column group of $\mathbf{B}$ has as many nonzero entries as the number of elements in Y^j.

Upon substitution of (35)-(37), (34) yields

$$\sum_{\alpha\in Y^m} \sum_{\beta=\alpha} (\mathbf{B}^*)_{m\alpha} \mathbf{W}_{\alpha\beta} \mathbf{B}_{\beta n} = \begin{cases} \sum_{\alpha\in Y^m} \mathbf{W}_{\alpha\alpha} & m = n \\ 0 & m \neq n. \end{cases}$$

Thus

$$(\mathbf{B}^*\mathbf{WB})_{mn} = \begin{cases} \sum_{\alpha\in Y^m} \mathbf{W}_{\alpha\alpha} & m = n \\ 0 & m \neq n \end{cases}, \; m, n=1,2,\ldots NMN$$

- 23 -

Since $\mathbf{W}_{\alpha\alpha} \in \Re(NDN, NDN)$ is symmetric and independent of $\mathbf{k}$, so is $\mathbf{B}^*\mathbf{W}\mathbf{B}$.

End of proof of Proposition 1.

Proposition 2. For a representative cell of a 2D periodic lattice structure, the stiffness matrix $\mathbf{K}$ and mass matrix $\mathbf{M}$ defined by (20) and (19) are Hermitian.

Proof:

Taking Hermitian transpose of both sides of (19), it follows that

$$\mathbf{M}^* = (\mathbf{M}^{mm})^* + (\mathbf{B}^*\mathbf{M}^{sm})^* + (\mathbf{M}^{ms}\mathbf{B})^* + (\mathbf{B}^*\mathbf{M}^{ss}\mathbf{B})^*$$

$$= (\mathbf{M}^{mm})^* + (\mathbf{M}^{sm})^*\mathbf{B} + \mathbf{B}^*(\mathbf{M}^{ms})^* + \mathbf{B}^*(\mathbf{M}^{ss})^*\mathbf{B}$$

Applying the properties of $\mathbf{M}^{cell}$ and $\mathbf{S}^{cell}$ (see Section 3.3), we have

$$\mathbf{M}^* = \mathbf{M}^{mm} + \mathbf{B}^*\mathbf{M}^{sm} + \mathbf{M}^{ms}\mathbf{B} + \mathbf{B}^*\mathbf{M}^{ss}\mathbf{B} = \mathbf{M}$$

Similarly

$$\mathbf{K}^* = \mathbf{K}$$

End of proof of Proposition 2.

Proposition 3. Let $\partial(\ )$ denote $\dfrac{\partial(\ )}{\partial k_j}$ (j=1, 2), λ_i denote a distinct eigenvalue of (26) and $\mathbf{a}_i$ denote its corresponding eigenvector normalized with respect to the mass matrix $\mathbf{M}$. If we assume sufficient differentiability of all parameters, then for a representative cell of a 2D periodic lattice structure with Hermitian stiffness matrix $\mathbf{K}$ (20) and mass matrix $\mathbf{M}$ (19),

$$\partial\lambda_i = \mathbf{a}_i^*(\partial\mathbf{K} - \lambda_i\partial\mathbf{M})\mathbf{a}_i \tag{38}$$

where

$$\partial \mathbf{M} = \partial \mathbf{B}^* \mathbf{M}^{sm} + \mathbf{M}^{ms} \partial \mathbf{B} \tag{39}$$

$$\partial \mathbf{K} = \partial \mathbf{B}^* \mathbf{S}^{sm} + \mathbf{S}^{ms} \partial \mathbf{B} \tag{40}$$

and $\partial \mathbf{M}$ and $\partial \mathbf{K}$ are Hermitian.

Proof:

Equation (38) is a well-known formula. The derivation of (39) and (40) is shown in the following.

Since $\mathbf{S}^{ss}$ and $\mathbf{M}^{ss}$ are block diagonal with symmetric sub-matrices of order NDN x NDN (see Section 3.3), it follows from Proposition 1 that

$$\partial (\mathbf{B}^* \mathbf{S}^{ss} \mathbf{B}) = 0 \tag{41}$$

$$\partial (\mathbf{B}^* \mathbf{M}^{ss} \mathbf{B}) = 0 \tag{42}$$

Taking derivative of both sides of (19) and (20) with respect to $\mathbf{k}$, applying (41) and (42) and noting that only $\mathbf{B}$ is a function of $\mathbf{k}$, it follows that

$$\partial \mathbf{M} = \partial \mathbf{B}^* \mathbf{M}^{sm} + \mathbf{M}^{ms} \partial \mathbf{B}$$

and

$$\partial \mathbf{K} = \partial \mathbf{B}^* \mathbf{S}^{sm} + \mathbf{S}^{ms} \partial \mathbf{B}$$

Taking Hermitian transpose of both sides of (39), it follows that

$$(\partial \mathbf{M})^* = (\partial \mathbf{B}^* \mathbf{M}^{sm})^* + (\mathbf{M}^{ms} \partial \mathbf{B})^*$$

$$= \partial \mathbf{B}^* \mathbf{M}^{sm} + \mathbf{M}^{ms} \partial \mathbf{B} = \partial \mathbf{M}$$

Similarly

$$(\partial \mathbf{K})^* = \partial \mathbf{K}$$

End of proof of Proposition 3.

Proposition 4. Let β ($\beta \in \{1,2,...NSN\}$) denote an arbitrary slave node in a representative cell, $\mathbf{n}_\beta$ denote the cell number for the cell in which β is a master node, and Ξ denote the cell number set of the cells in which the slave nodes of a representative cell are master nodes, i.e. $\Xi = \{\mathbf{n}_\beta : \beta = 1,2,...NSN\}$. If $\sin(\mathbf{k} \bullet \mathbf{n}_\beta) = 0$ for $\forall$ $\mathbf{n}_\beta \in \Xi$, where $\mathbf{k} \in \Re^2$, then $\partial\lambda_i = 0$ and the eigenvector $\mathbf{a}_i$ associated with the distinct eigenvalue λ_i is real.

Proof:

If $\sin(\mathbf{k} \bullet \mathbf{n}_\beta) = 0$ for $\forall$ $\mathbf{n}_\beta \in \Xi$, then $e^{i\mathbf{k} \bullet \mathbf{n}_\beta}$ is real, since

$$e^{i\mathbf{k} \bullet \mathbf{n}_\beta} = \cos(\mathbf{k} \bullet \mathbf{n}_\beta) + i\sin(\mathbf{k} \bullet \mathbf{n}_\beta) = \cos(\mathbf{k} \bullet \mathbf{n}_\beta)$$

It follows from (33) that $\mathbf{B}_{\beta j}$ is real. Moreover $\partial(\mathbf{B}_{\beta j})$ is pure imaginary since

$$\frac{\partial e^{i\mathbf{k} \bullet \mathbf{n}_\beta}}{\partial k_l} = i n_{\beta l} e^{i\mathbf{k} \bullet \mathbf{n}_\beta} , l=1, 2$$

It follows that the quasi-periodicity matrix $\mathbf{B}$ is real and $\partial\mathbf{B}$ is pure imaginary.

Since $\mathbf{B}$ is real, it follows from (19) and (20) that $\mathbf{K}$ and $\mathbf{M}$ are real. Further, applying Proposition 2, $\mathbf{K}$ and $\mathbf{M}$ are real and symmetric. Therefore the eigenvalues λ_i and eigenvectors $\mathbf{a}_i$ are real.

Since $\partial\mathbf{B}$ is pure imaginary, it follows from Proposition 3 that $\partial\mathbf{M}$ and $\partial\mathbf{K}$ are skew-symmetric. Therefore, $\partial\mathbf{K} - \lambda_i\partial\mathbf{M}$ is skew-symmetric because of the fact that λ_i is real. It follows from (38) that

$$\partial\lambda_i = \mathbf{a}_i^T (\partial\mathbf{K} - \lambda_i\partial\mathbf{M})\mathbf{a}_i = 0$$

End of proof of Proposition 4.

For the examples studied in this work, $\Xi = \{(1,0)^T, (0,1)^T\}$. The critical points A, B and C are associated with $\mathbf{k} = (\pi, \pi)$, $(0, 0)$ and $(\pi, 0)$. It follows from Proposition 4 that these critical points are stationary points on the dispersion diagram and the eigenvectors associated with the distinct eigenvalues at these critical points are real. Real eigenvectors represent standing waves and they are associated with energy bounds that can be transmitted through periodic structures. This discussion helps explain why the bounds of the optimal gaps in the examples given in the later chapters are obtained at the critical points when the eigenvalues at the bounds of the optimal gaps are distinct.

Chapter 4   Optimization of Infinite 2D Periodic Grids

4.1   Optimization Problem Formulations

In this section, two optimization problem formulations are presented to design 2D periodic grid structures with maximum band gaps. In the first formulation, the band gap is maximized by adding additional (lumped) masses to certain nodes ("Design nodes"). In the second formulation, by assuming a circular cross section for the grid elements, we also change the cross section radii of certain grid elements ("Design elements"). In this formulation, the mass and stiffness of the structure are changed simultaneously.

4.1.1   Formulation 1: Additional Mass as Design Variables

In this formulation, the band gap in 2D periodic grid structures is maximized by adding additional (lumped) masses to certain nodes of the representative cell, called here the "design nodes". The optimization problem is

$$\max_{\mathbf{x} \in \mathbf{X}_1} G(\mathbf{x}) = \min_{\mathbf{k} \in \Psi} \lambda_{j+1}(\mathbf{k}, \mathbf{x}) - \max_{\mathbf{k} \in \Psi} \lambda_j(\mathbf{k}, \mathbf{x}) \qquad (43)$$

Here $\mathbf{x} = \{x_i\}$, $i=1,\ldots, n$, denotes the vector of design variables and x_i is the nonstructural mass to be added to the ith design node. $\mathbf{X}_1$ is the feasible set, in this case,

$$\mathbf{X}_1 = \{\mathbf{x} \in \Re^n : 0 \le x_i \le x_{\max} = \beta m_{cell}, \Sigma x_i \le \Lambda x_{\max}\} \qquad (44)$$

where n is the number of design variables, and β, m_{cell}, Λ and $x_{\max}$ are prescribed positive real numbers that control the total amount of nonstructural material to be added to the cell. The objective function $G(\mathbf{x})$ is the band gap size between bands j and $j+1$.

$\lambda_j(\mathbf{k},\mathbf{x})$ and $\lambda_{j+1}(\mathbf{k},\mathbf{x})$ are the jth and $(j+1)$th eigenvalue bands of the generalized eigenvalue problem

$$(\mathbf{K}(\mathbf{k}) - \lambda\mathbf{M}(\mathbf{k},\mathbf{x}))\mathbf{a} = 0, \quad \mathbf{k} \in \Psi \text{ and } \mathbf{x} \in X_1 \tag{45}$$

Note that since adding masses to the nodes of a structure does not change the structure's stiffness, the stiffness matrix $\mathbf{K}$ is independent of $\mathbf{x}$ for formulation 1.

4.1.2   Formulation 2: Both Additional Mass and Element Radii as Design Variables

As the second formulation, we consider both additional nonstructural masses at the design nodes and the cross section radii of the design elements as design variables. The optimization problem is

$$\max_{\mathbf{x} \in X_2} G(\mathbf{x}) = \min_{\mathbf{k}} \lambda_{j+1}(\mathbf{k},\mathbf{x}) - \max_{\mathbf{k}} \lambda_j(\mathbf{k},\mathbf{x})$$

where $\mathbf{x} = \{\mathbf{x}^1, \mathbf{x}^2\}$, $\mathbf{x}^1 = \{x_i^1\}$ and x_i^1 is the additional nonstructural mass to be added to the ith design node, $\mathbf{x}^2 = \{x_j^2\}$ and x_j^2 is the cross-section radius of the jth design element. In this case, the feasible set is

$$X_2 = \{\mathbf{x}^1 \in \Re^n \text{and } \mathbf{x}^2 \in \Re^p : 0 \le x_i^1 \le x_{\max} = \beta m_{cell}, \sum x_i^1 \le \Lambda m_{cell}, r_{\min} \le x_j^2 \le r_{\max}\}$$

Here n is number of design nodes, p is number of design elements, $r_{\min}$ and $r_{\max}$ are lower and upper bounds of the cross section radii of design elements. $\lambda_j(\mathbf{k},\mathbf{x})$ and $\lambda_{j+1}(\mathbf{k},\mathbf{x})$ are the jth and $(j+1)$th eigenvalue bands of the generalized eigenvalue problem

$$(\mathbf{K}(\mathbf{k},\mathbf{x}^2) - \lambda\mathbf{M}(\mathbf{k},\mathbf{x}))\mathbf{a} = 0, \mathbf{k} \in \Psi \text{ and } \mathbf{x} \in X_2$$

To make this problem computationally easier to solve, we consider a *modified* formulation that studies the effect of changing the bar radii on the *stiffness only* (the structural mass is kept constant at the reference value). In this case the above problem is replaced by

$$(\mathbf{K}(\mathbf{k},\mathbf{x}^2) - \lambda\mathbf{M}(\mathbf{k},\mathbf{x}^1))\mathbf{a} = 0, \mathbf{k} \in \Psi \text{ and } \mathbf{x} \in X_2 \tag{46}$$

4.2   Numerical Implementation Issues of the Optimization Problems

4.2.1   Numerical Implementation

To solve the above optimization problems numerically, the subset of the irreducible Brillouin zone, Ψ=[A-B-C-A] (Figure 4), is discretized at m sample points and the discrete set is denoted by

$$\hat{\Psi} = \{\mathbf{k}_1, \mathbf{k}_2, \cdots, \mathbf{k}_m\}, \mathbf{k}_i \in \Psi, i = 1, \ldots, m. \tag{47}$$

For fixed $\mathbf{x}$, this introduces discrete values of gap sizes between eigenvalues evaluated at two pairs of wave vectors ($\mathbf{k}_p$ and $\mathbf{k}_q$) in $\hat{\Psi}$. Gap sizes between bands j and $j+1$ on the discrete domain can be described by the quantities

$$G_{pq}(\mathbf{x}) = \lambda_{j+1}(\mathbf{k}_p, \mathbf{x}) - \lambda_j(\mathbf{k}_q, \mathbf{x}), \mathbf{k}_p, \mathbf{k}_q \in \hat{\Psi}, p, q = 1, \ldots, m \tag{48}$$

Then the optimization problems are reduced to

$$\max_{\mathbf{x} \in \mathbf{X}_i} \min_{1 \le p, q \le m} G_{pq}(\mathbf{x}), i = 1,2 \tag{49}$$

Problem (49) can be written as follows:

Find $\mathbf{x} \in \mathfrak{R}^n$ and $z \in \mathfrak{R}$ that

maximize z

subject to $G_{pq}(\mathbf{x}) \ge z$, $\mathbf{x} \in \mathbf{X}_i$, i=1, 2 \tag{50}

- 30 -

Problem (50) is solved numerically using the method of moving asymptotes [19]. To facilitate computations, an active set of strategy is introduced so that a sequence of problems is solved by considering only a *subset* of the most critical constraints in (49), once a time. To avoid introducing redundant constraints, at most *n* of the most critical constraints are kept each time (*n* represents the total number of design variables). As the algorithm converges, feasibility of the solution is verified against the *complete* set of constraints.

The gradient of $G_{pq}(\mathbf{x})$ with respect to the design variable $\mathbf{x}$ is computed using well-known formulas. Letting $(\ )^{\nabla}$ denote $\dfrac{\partial(\ )}{\partial \mathbf{x}}$,

$$G_{pq}{}^{\nabla} = (\lambda_{j+1}(\mathbf{k}_p, \mathbf{x}))^{\nabla} - (\lambda_j(\mathbf{k}_q, \mathbf{x}))^{\nabla} \tag{51}$$

where

$$\lambda_i^{\nabla} = \mathbf{a}_i^* \mathbf{K}^{\nabla} \mathbf{a}_i - \lambda_i \mathbf{a}_i^* \mathbf{M}^{\nabla} \mathbf{a}_i \tag{52}$$

and $\mathbf{a}_i$ is normalized with respect to the mass matrix $\mathbf{M}$. (52) holds only for distinct eigenvalues.

In (52) λ_i and $\mathbf{a}_i$ can be obtained from the current design. The procedures of computing $G_{pq}{}^{\nabla}$ for the above two optimization formulations are described in the following sections.

4.2.2 Derivative of Gap Size with Respect to Nonstructural Mass Variables

Since adding non-structural masses does not change the stiffness of the structure,

$$\mathbf{K}^{\nabla} = \mathbf{0} \tag{53}$$

Furthermore, since the design variable x_h only appears along the diagonal of $\mathbf{M}$, at the position corresponding to the translation degree of freedom of design node h, $\dfrac{\partial \mathbf{M}}{\partial x_h}$ has only one nonzero entry. So (52) yields

$$\frac{\partial \lambda_i}{\partial x_h} = -\lambda_i (\mathbf{a}_i^h)^* \mathbf{a}_i^h = -\lambda_i \left\| \mathbf{a}_i^h \right\|^2 \tag{54}$$

where $\mathbf{a}_i^h$ represents the component corresponding to the translation degree of freedom of design node h in the mass-normalized eigenvector $\mathbf{a}_i$.

Once $\dfrac{\partial \lambda_i}{\partial x_h}$ is computed using (54), the gradient $G_{pq}{}^{\nabla}$ can be obtained from (51)

4.2.3 Derivative of Gap Size with Respect to Element Radius Variables

Recalling the FE stiffness matrix and mass matrix formulation procedure in Chapter 3, for a grid element with circular cross section of radius r, the geometry properties in (6) and (7) are given in terms of r by

$$A = \pi r^2 \tag{55}$$

$$I = \frac{\pi r^4}{4} \tag{56}$$

$$J = \frac{\pi r^4}{2} \tag{57}$$

Substituting (55) through (57) into (6) and (7) and taking derivative with respect to r, it follows that

$$\frac{\partial (\hat{\mathbf{S}}^e)}{\partial r} = \frac{4}{r} \hat{\mathbf{S}}^e \tag{58}$$

$$\frac{\partial(\hat{\mathbf{M}}^e)}{\partial r} = \frac{2}{r}\mathbf{P}\hat{\mathbf{M}}^e \tag{59}$$

where $\mathbf{P}$ is a constant matrix and given by

$$\mathbf{P} = \begin{bmatrix} 1 & 0 & 0 & 0 & 0 & 0 \\ 0 & 2 & 0 & 0 & 0 & 0 \\ 0 & 0 & 1 & 0 & 0 & 0 \\ 0 & 0 & 0 & 1 & 0 & 0 \\ 0 & 0 & 0 & 0 & 2 & 0 \\ 0 & 0 & 0 & 0 & 0 & 1 \end{bmatrix} \tag{60}$$

Since the local to global transformation matrix $\mathbf{L}$ (see (8)) is independent of radius r, it follows from (9) and (10) that

$$\frac{\partial \mathbf{S}^e}{\partial r} = \mathbf{L}^T \frac{\partial(\hat{\mathbf{S}}^e)}{\partial r}\mathbf{L} \tag{61}$$

$$\frac{\partial \mathbf{M}^e}{\partial r} = \mathbf{L}^T \frac{\partial(\hat{\mathbf{M}}^e)}{\partial r}\mathbf{L} \tag{62}$$

Upon inserting (58) and (59) into (61) and (62) and applying $\mathbf{L}^{-1} = \mathbf{L}^T$, the derivatives of element stiffness and mass matrices with respect to radius r are found to be

$$\frac{\partial \mathbf{S}^e}{\partial r} = \frac{4}{r}\mathbf{S}^e \tag{63}$$

$$\frac{\partial \mathbf{M}^e}{\partial r} = \frac{2}{r}\mathbf{Q}\mathbf{M}^e \tag{64}$$

where

$$\mathbf{Q} = \mathbf{L}^T\mathbf{P}\mathbf{L} \tag{65}$$

Substituting (8) and (60) into (65), it follows that

- 33 -

$$\mathbf{Q} = \begin{bmatrix} 1 & 0 & 0 & 0 & 0 & 0 \\ 0 & 1+\cos^2\theta & \cos\theta\sin\theta & 0 & 0 & 0 \\ 0 & \cos\theta\sin\theta & 1+\sin^2\theta & 0 & 0 & 0 \\ 0 & 0 & 0 & 1 & 0 & 0 \\ 0 & 0 & 0 & 0 & 1+\cos^2\theta & \cos\theta\sin\theta \\ 0 & 0 & 0 & 0 & \cos\theta\sin\theta & 1+\sin^2\theta \end{bmatrix} \tag{66}$$

where θ is defined in (8).

After computing $\dfrac{\partial \mathbf{S}^e}{\partial r}$ and $\dfrac{\partial \mathbf{M}^e}{\partial r}$, the derivatives of the global stiffness and mass

matrices with respect to design element radius variable r, $\dfrac{\partial \mathbf{S}^{cell}}{\partial r}$ and $\dfrac{\partial \mathbf{M}^{cell}}{\partial r}$, are

obtained following a standard FEM assembly procedure. Then $\dfrac{\partial \mathbf{K}}{\partial r}$ and $\dfrac{\partial \mathbf{M}}{\partial r}$ are

computed using the derivative forms of (19) and (20). Finally, λ_i^∇ and $G_{pq}{}^\nabla$ can be

obtained from (52) and (51). In a modified version of formulation 2, we keep the

structural mass constant and set $\dfrac{\partial \mathbf{M}}{\partial r} = 0$.

Chapter 5 Examples of Optimization Problems

5.1 Examples

Using formulation 1 and formulation 2, band gaps are introduced and maximized in infinite 2D grid structures with a 6x6 representative square cell (Figure 6) and a 6x6 representative skew cell (Figure 7). The tiling vectors of the representative cells are

$$\mathbf{t}^{(1)} = (6L,0)^T \text{ and } \mathbf{t}^{(2)} = 6L(\cos\alpha, \sin\alpha)^T$$

where $6L$=60mm and L is the length of each bar (grid element), and the angle between the two tiling vectors α=90° for square cell and α=45° for skew cell respectively. Material properties are: E=5.28 GPa, G=1.98 GPa and ρ=1200 kg/m^3 . The radius of the cylindrical bar of the homogeneous structures is $r_0 = 0.5$mm .

(a) Square cell   (b) Tiling vectors
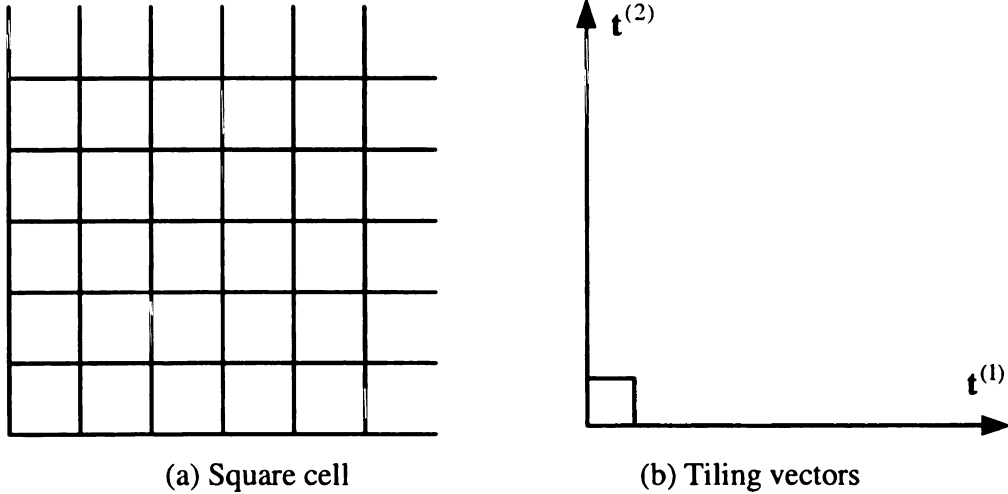
Figure 6. Homogeneous 6x6 representative square cell

| (a) Skew Cell | (b) Tiling vectors |
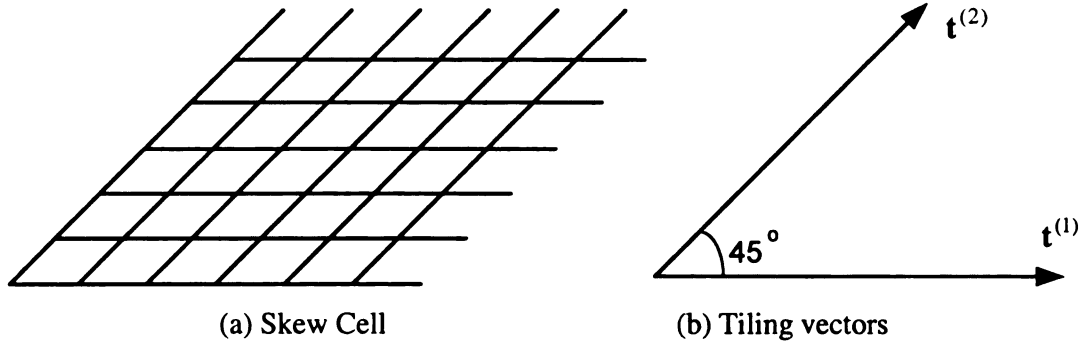
Figure 7. Homogeneous 6x6 representative skew cell

5.1.1 Examples of Square Structures Using Formulation 1

In this section, band gaps above band 1 and band 3 are introduced and maximized in

infinite 2D periodic grid structures with a 6×6 representative square cell using different

values of Λ and x_{max} (recall that Λ limits total mass added to the structure through the

constraint $\sum x_i \leq \Lambda x_{max}$). The potential locations where non-structural masses can be

placed are shown in Figure 8 (nodes denoted by the squares). By assuming the

symmetries defined in (30) of the optimal solutions so that Ψ (Figure 4) can be used to

obtain all eigenfrequencies of the periodic structure, only three design masses (labeled 1,

2, and 3 in Figure 8) to be added to their respective nodes are needed.
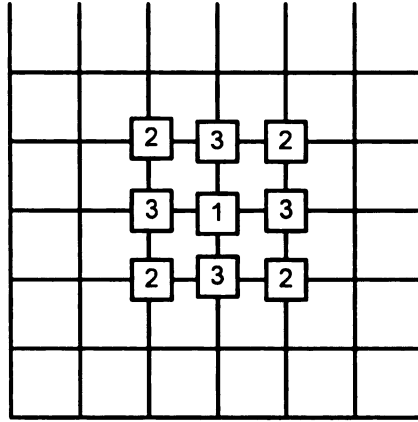
Figure 8. Locations of additional (design) masses for square cell in Formulation 1

The design constraints, optimal mass distributions, and their corresponding gap sizes are given in Table 1. For the local optima with optimal band gaps, the optimal mass distribution graphs and dispersion diagrams are shown in Figure 9 through Figure 14.

For all the optimal designs with optimal band gaps above band 1, the mass (x_1) added to location 1 (center of the cell, Figure 8) reaches the upper bound (x_{max}) while no mass is placed at locations 2. If the total allowable mass constraint is set to allow only one mass to reach the upper bound, the total mass is always placed at location 1 for the optimal structures and increasing the upper bound constraint will create a bigger gap. Setting $\Lambda=9$ to remove the total allowable mass constraint, the optimal mass added to location 3 (x_3) decreases with the increase of the upper bound constraint (x_{max}). As evidenced from designs 3 and 5, adding mass *only* to location 1 reduces the lower bound of the optimal gap while keeps the upper bound of the gap fixed. However, adding mass to location 3 reduces the upper bound of the optimal gap as well as the lower bound of the optimal gap.

When one's goal is to maximize the gap above band 3, adding mass to location 3 becomes more advantageous. This is illustrated by the optimal result of design 8.

On the dispersion diagrams (Figure 9 through Figure 13) of all the optimal designs with optimal band gap above band 1, the lower bound of the band gap occurs at point A at which k=(π, π) and the upper bound of the band gap is achieved at point C associated with k=(π, 0).

Table 1. Local optima in examples of square structure using formulation 1 (α=90°)

Design No.	Constraints			Optimal Design		Optimal Gap		
	x_{max} $(\times m_{cell})$	Λ	Allow Total Mass Λx_{max}	Solution $\mathbf{x} = \{x_1, x_2, x_3\}$ $(\times m_{cell})$	Total Mass Used $(\times m_{cell})$	Gap Size (kHz)	Abv Band	Abv Freq. (kHz)
1	0.50	1	0.50	0.50 0.00 0.00	0.50	*	1	
2	0.50	9	4.50	0.50 0.00 0.50	2.50	1.0	1	3.1
3	0.80	1	0.80	0.80 0.00 0.00	0.80	0.6	1	4.5
4	0.80	9	7.20	0.80 0.00 0.31	2.04	1.1	1	3.3
5	1.00	1	1.00	1.00 0.00 0.00	1.00	1.0	1	4.1
6	1.00	9	9.00	1.00 0.00 0.16	1.64	1.2	1	3.5
7	0.50	9	4.50	0.02 0.50 0.50	4.02	*	3	
8	1.00	9	9.00	0.30 0.00 1.00	4.30	1.4	3	8.0

*No gap
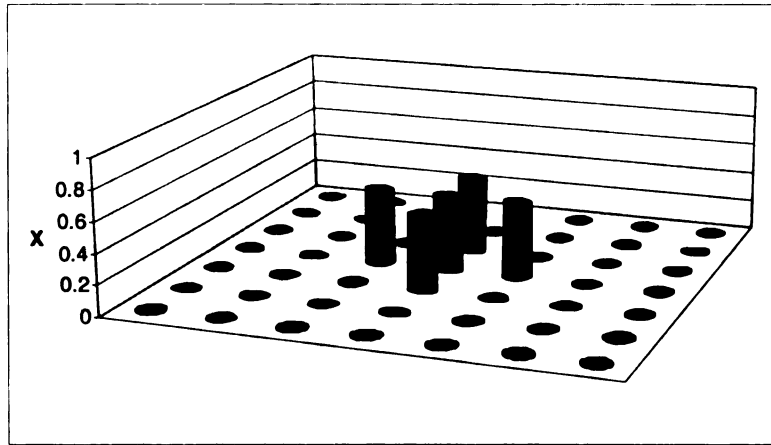
(a) Optimal mass distribution graph
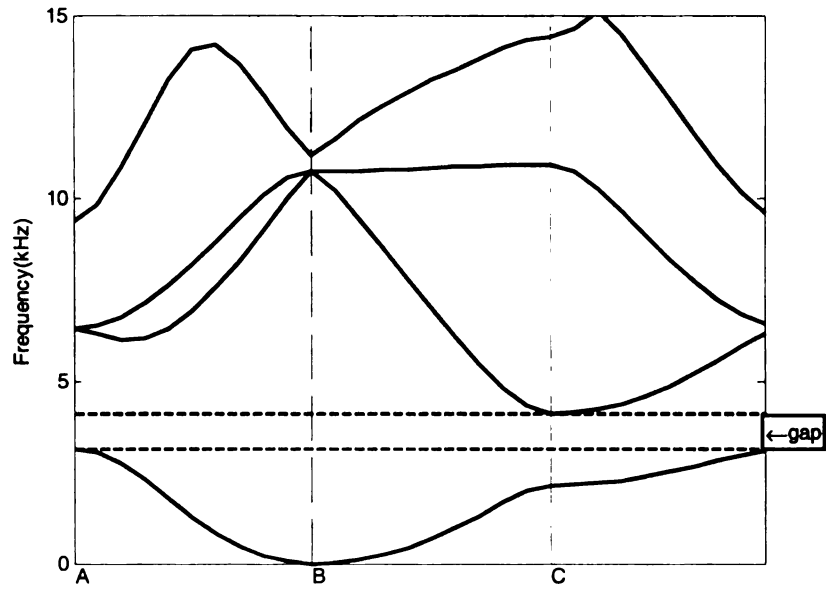
(b) Dispersion diagram

Figure 9. Mass distribution and dispersion diagram for design 2 in Table 1
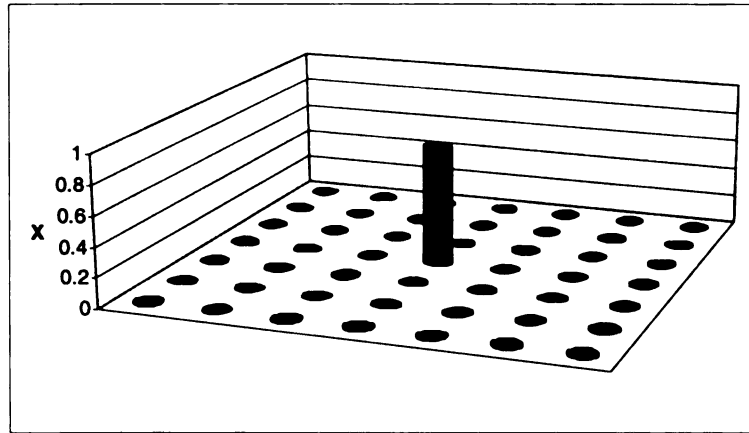
(a) Optimal mass distribution graph
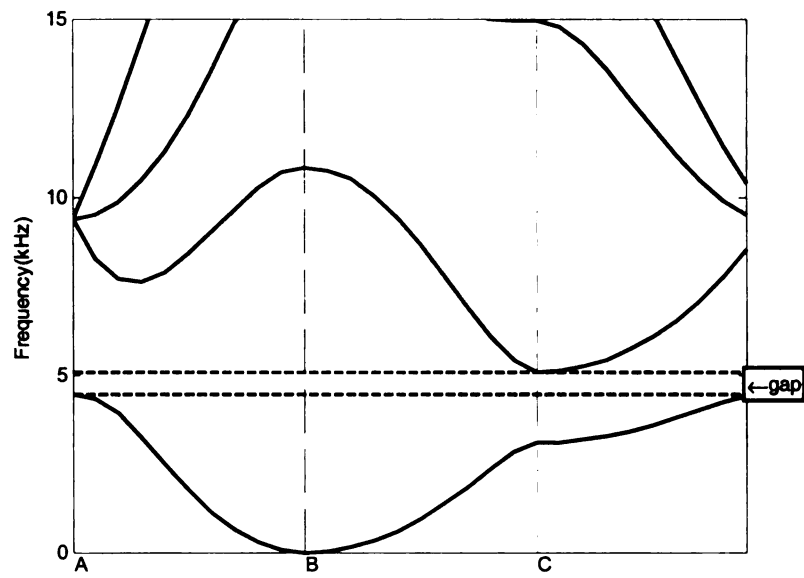
(b) Dispersion diagram

Figure 10. Mass distribution and dispersion diagram for design 3 in Table 1
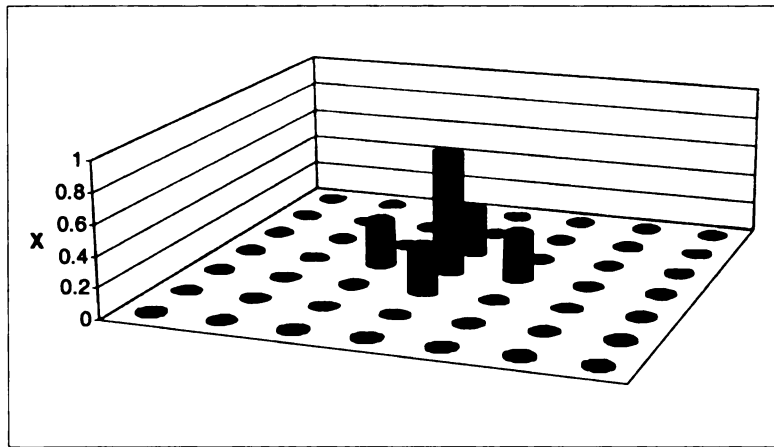
(a) Optimal mass distribution graph
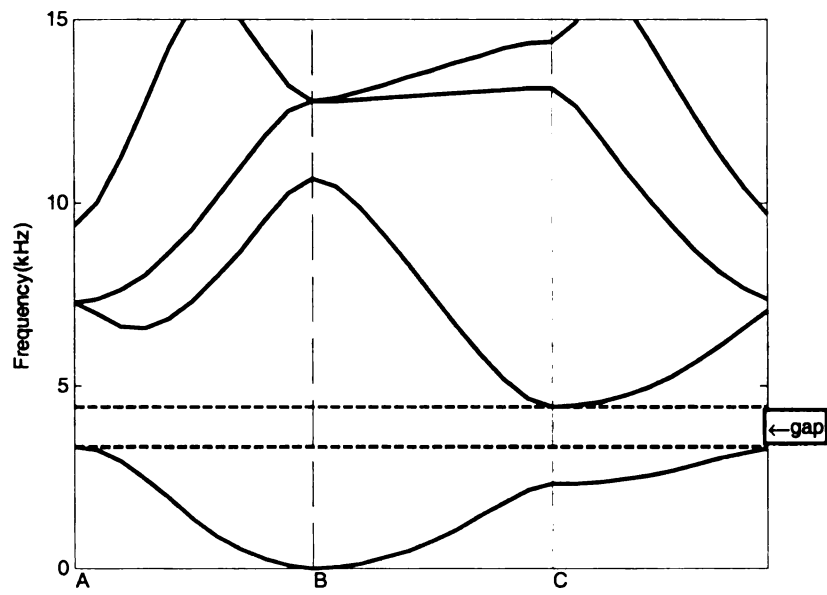
(b) Dispersion diagram

Figure 11. Mass distribution and dispersion diagram for design 4 in Table 1
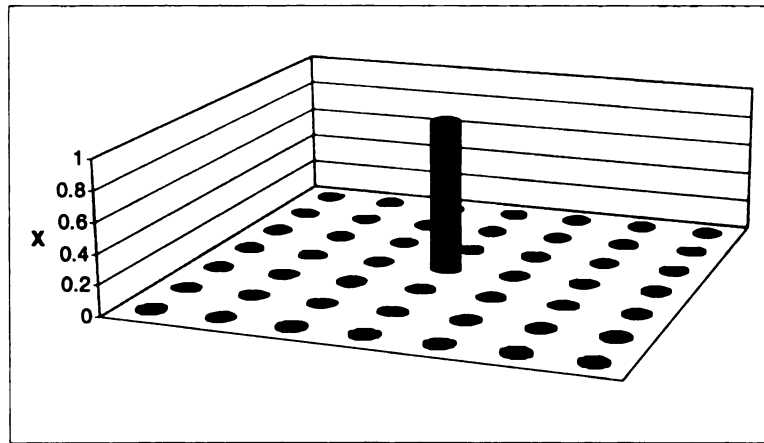
(a) Optimal mass distribution graph
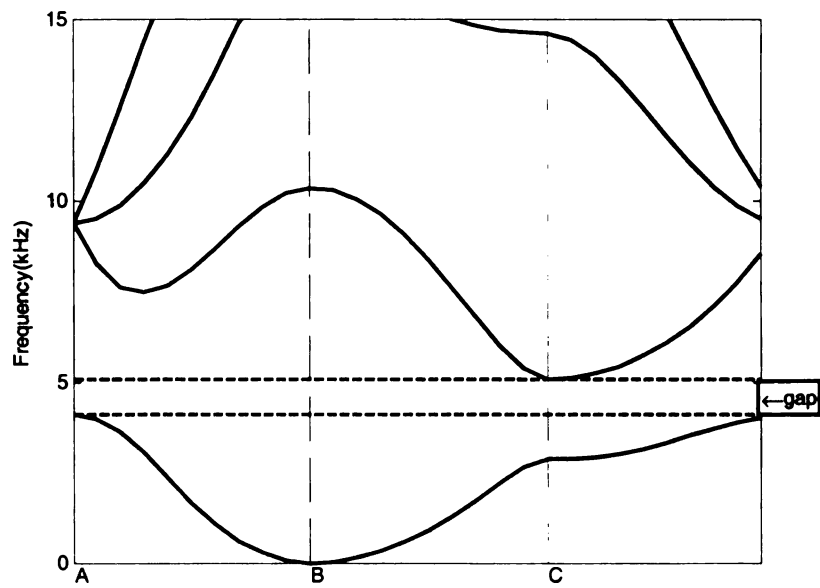
(b) Dispersion diagram

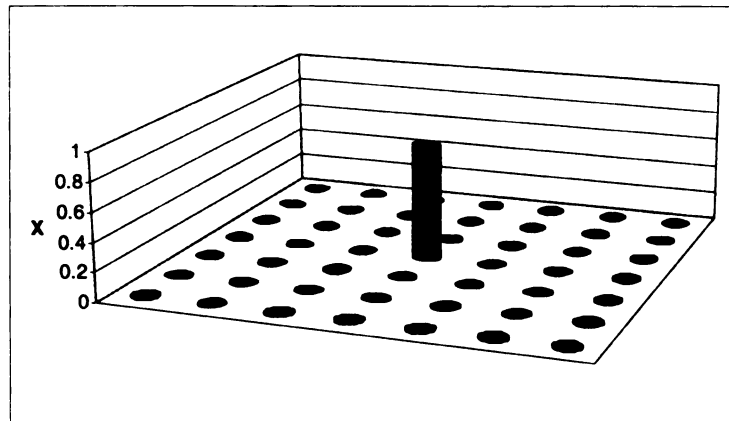Figure 12. Mass distribution and dispersion diagram for design 5 in Table 1
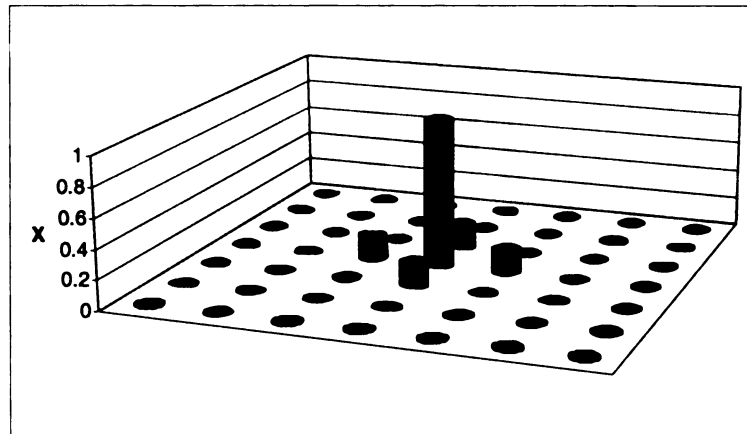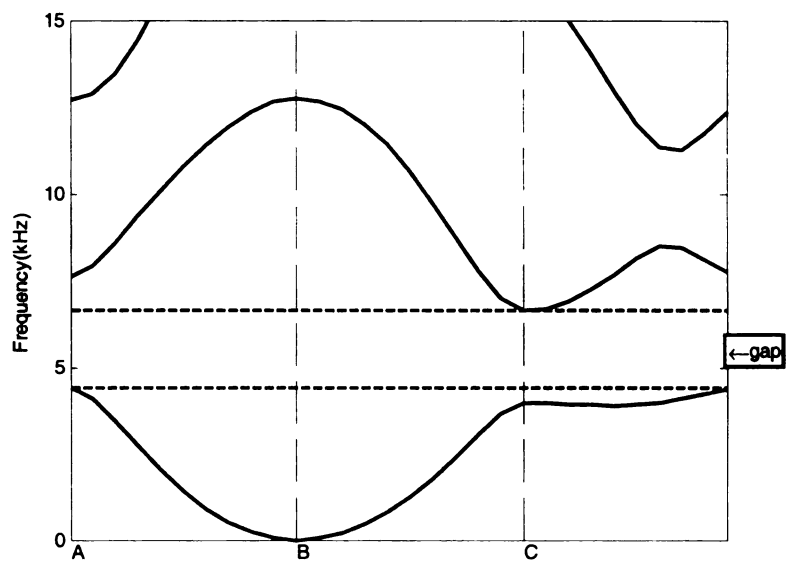
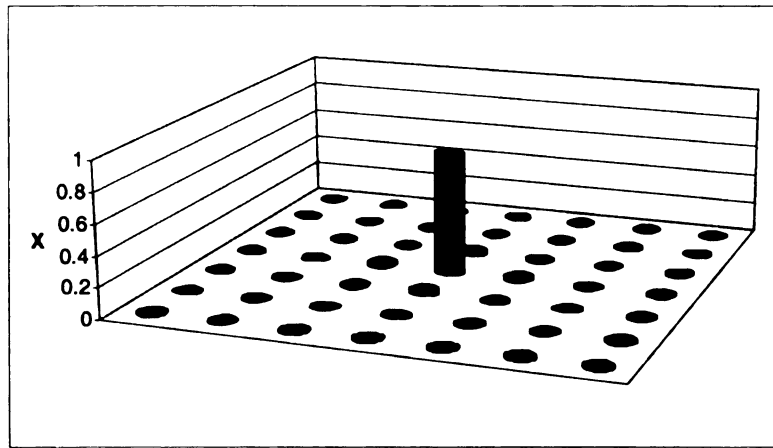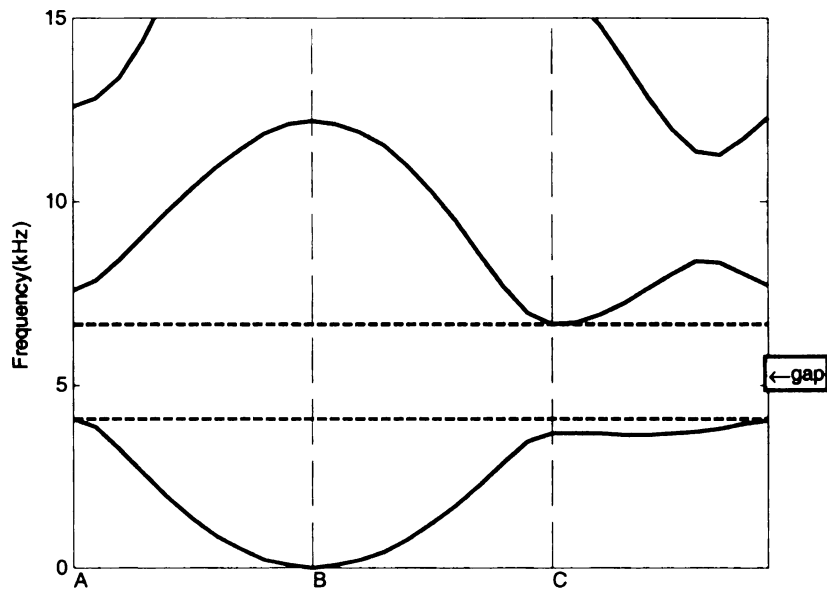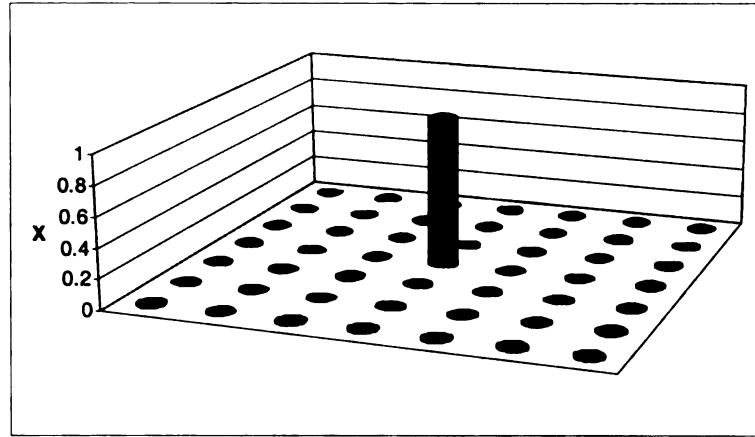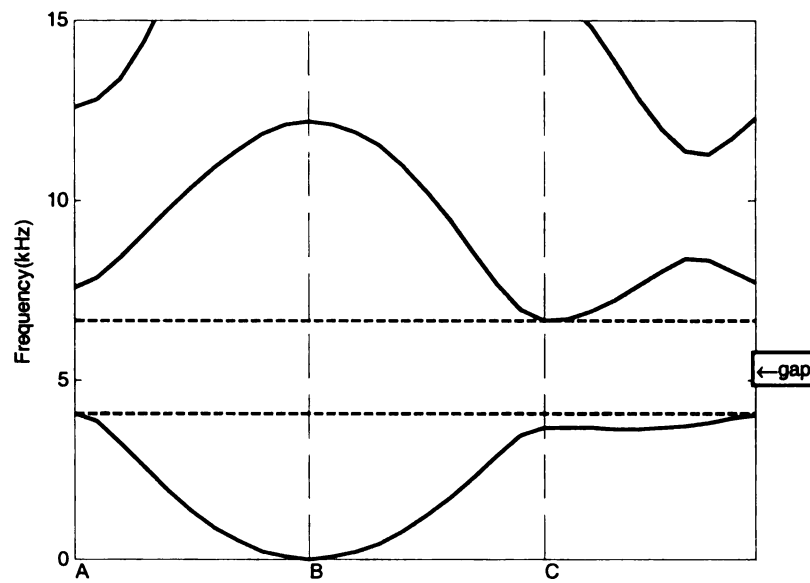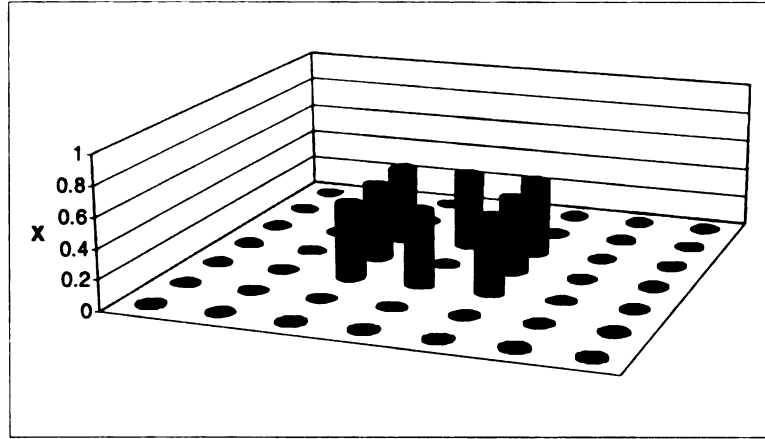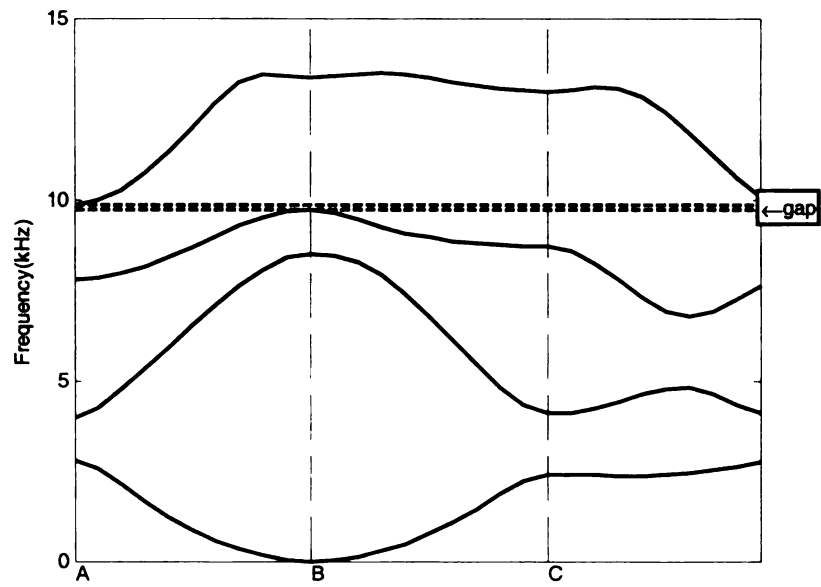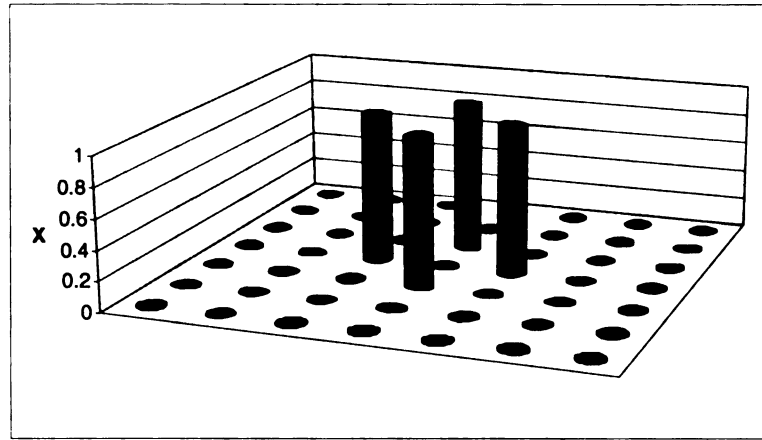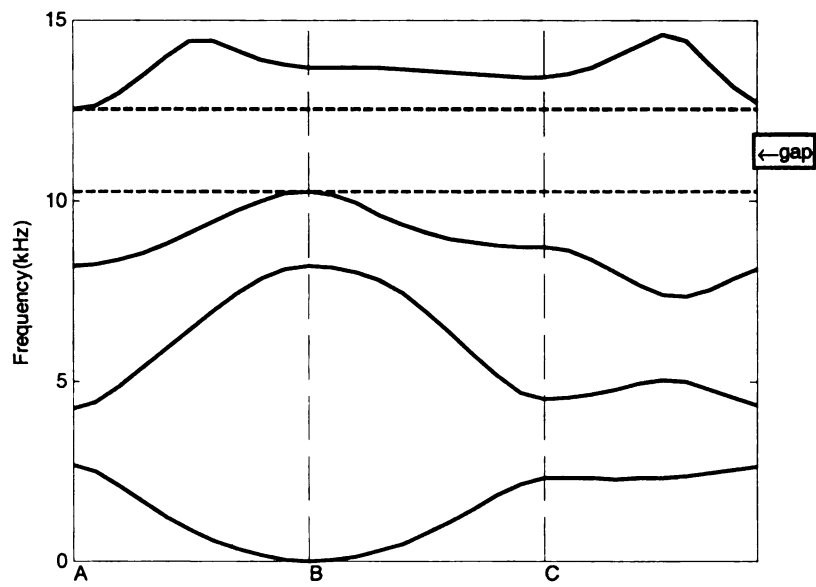(a) Optimal mass distribution graph
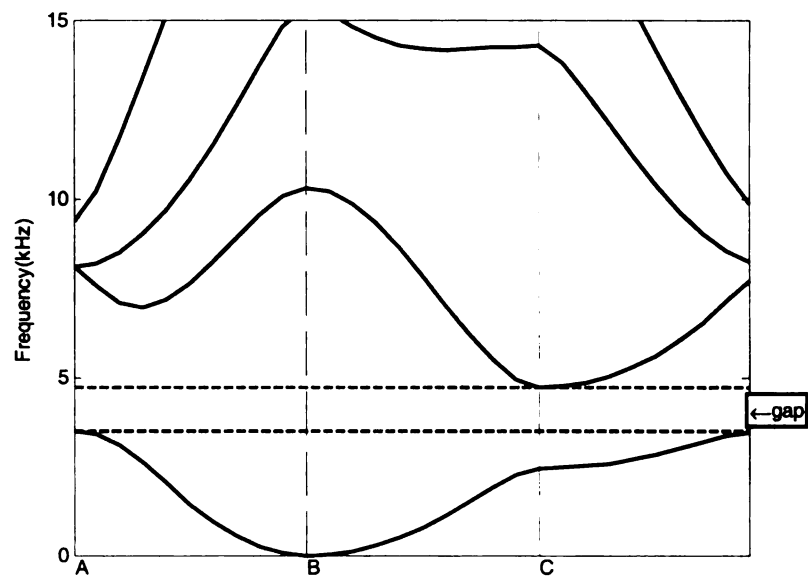
(b) Dispersion diagram

Figure 13. Mass distribution and dispersion diagram for design 6 in Table 1
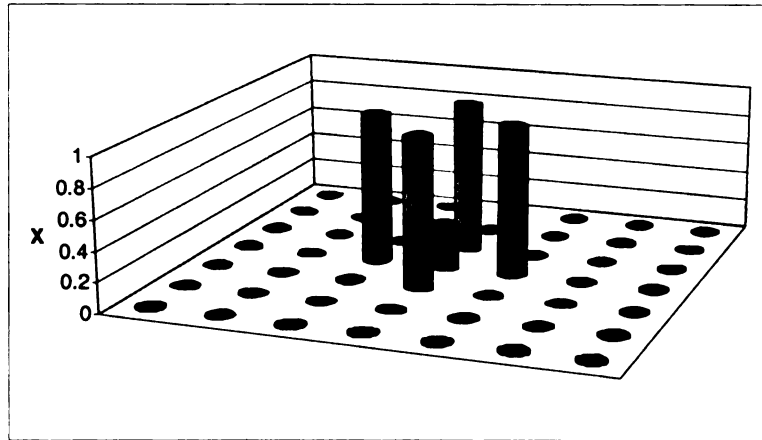
(a) Optimal mass distribution graph
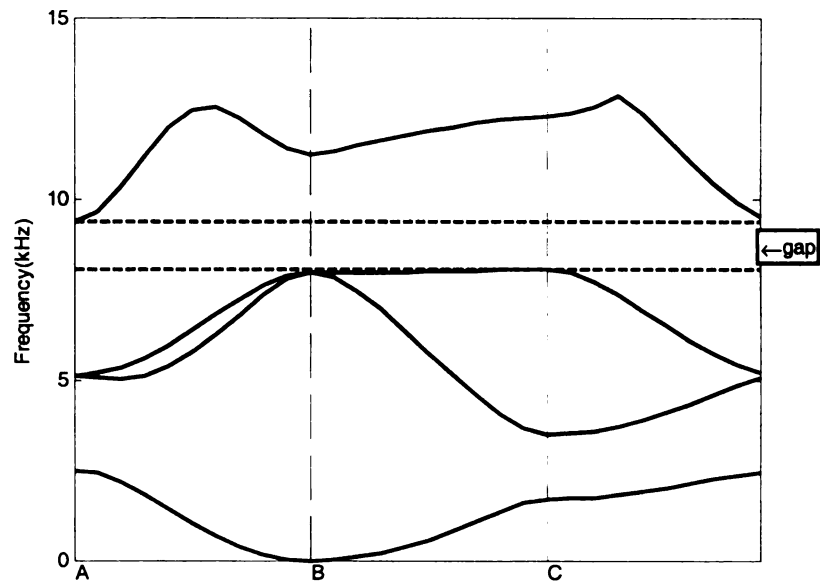
(b) Dispersion diagram

Figure 14. Mass distribution and dispersion diagram for design 8 in Table 1

5.1.2 Examples of Skew Structures Using Formulation 1

In this section, band gaps above band 1 and band 3 are introduced and maximized in infinite 2D periodic grid structures with a 6×6 representative skew cell (α=45°) using the same formulation and the same constraints as in Section 5.1.1. The potential locations where non-structural masses can be placed are shown in Figure 15. The results are shown in Table 2 and Figure 16 through Figure 22.
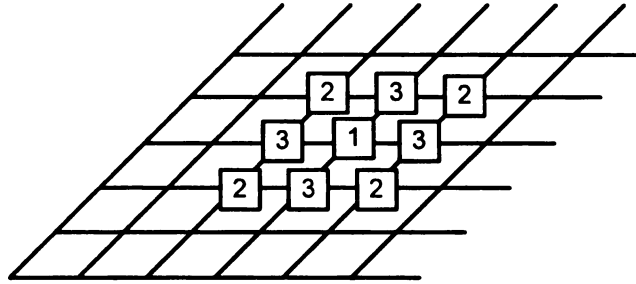
Figure 15. Locations of additional (design) masses for skew cell in Formulation 1

Table 2. Local optima in examples of skew structure using formulation 1 (α=45°)

Design No.	Constraints			Optimal Design		Optimal Gap		
	x_{max} $(\times m_{cell})$	Λ	Allow Total Mass Λx_{max}	Solution $\mathbf{x} = \{x_1, x_2, x_3\}$ $(\times m_{cell})$	Total Mass Used $(\times m_{cell})$	Gap Size (kHz)	Abv Band	Abv Freq. (kHz)
9	0.50	1	0.50	0.50 0.00 0.00	0.50	1.5	1	5.1
10	0.50	9	4.50	0.50 0.00 0.19	1.26	2.1	1	4.0
11	0.80	1	0.80	0.80 0.00 0.00	0.80	2.2	1	4.4
12	0.80	9	7.20	0.80 0.00 0.02	0.88	2.3	1	4.3
13	1.00	9	9.00	1.00 0.00 0.00	1.00	2.5	1	4.1
14	0.50	9	4.50	0.00 0.50 0.50	4.00	0.2	3	9.7
15	1.00	9	9.00	0.00 0.00 1.00	4.00	2.2	3	10.3

Given the same constraints as those for the examples in Table 1, similar optimal mass distributions are obtained but the band gaps are much larger in skew structures (Table 2)
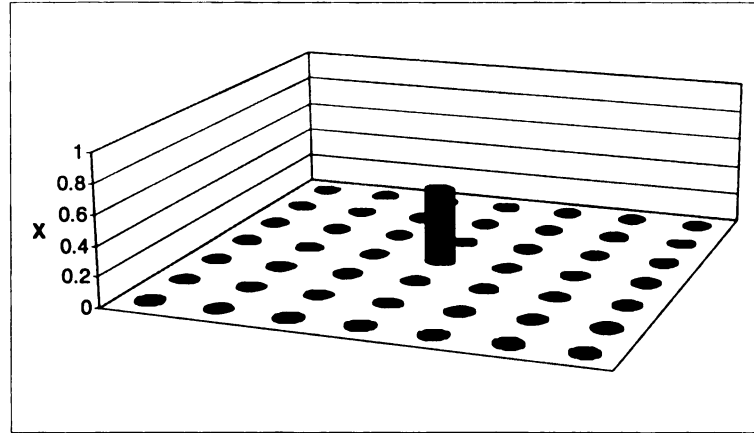
(a) Optimal mass distribution graph
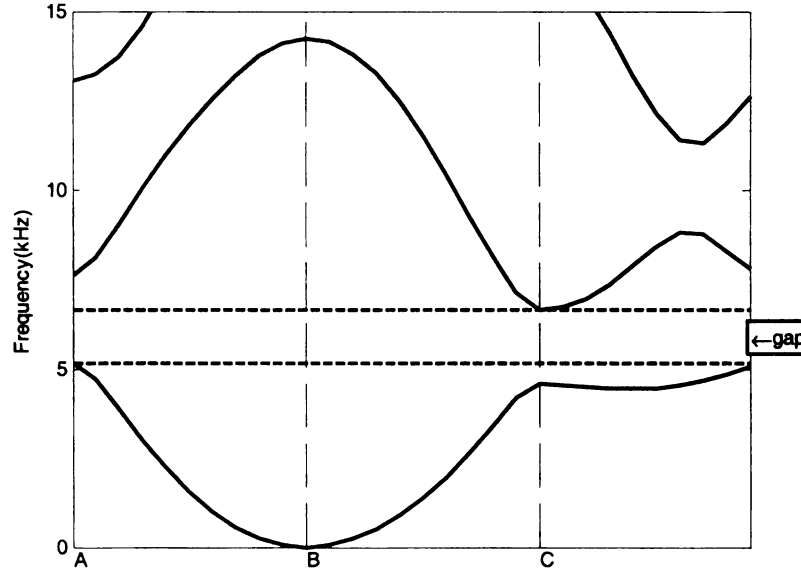
(b) Dispersion diagram

Figure 16. Mass distribution and dispersion diagram for design 9 in Table 2.

than those in square structures (Table 1). Especially, changing α from 90° to 45° can increase the upper bounds of the optimal gaps above band 1 significantly. Design 11 has the same mass distribution as design 3 but the upper bound of the optimal gap of one is 30% higher than that of the other (The same is true for design 13 and 5). All other

observations discussed in Section 5.1.1 about the optimal solution for square structures apply to the optimal solutions of skew structures in this section.
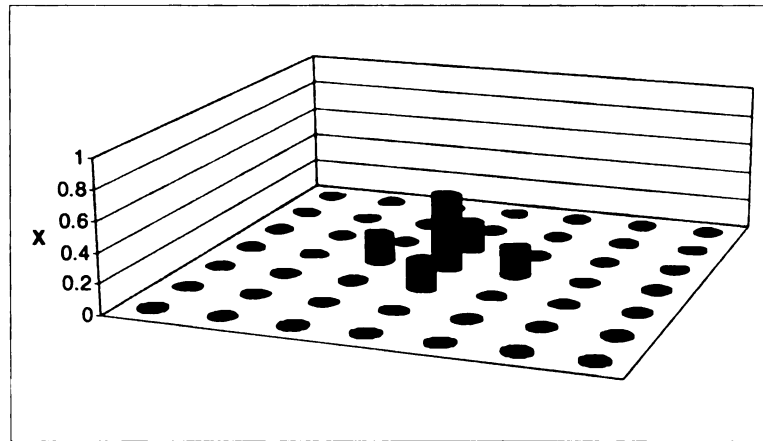
(a) Optimal mass distribution graph
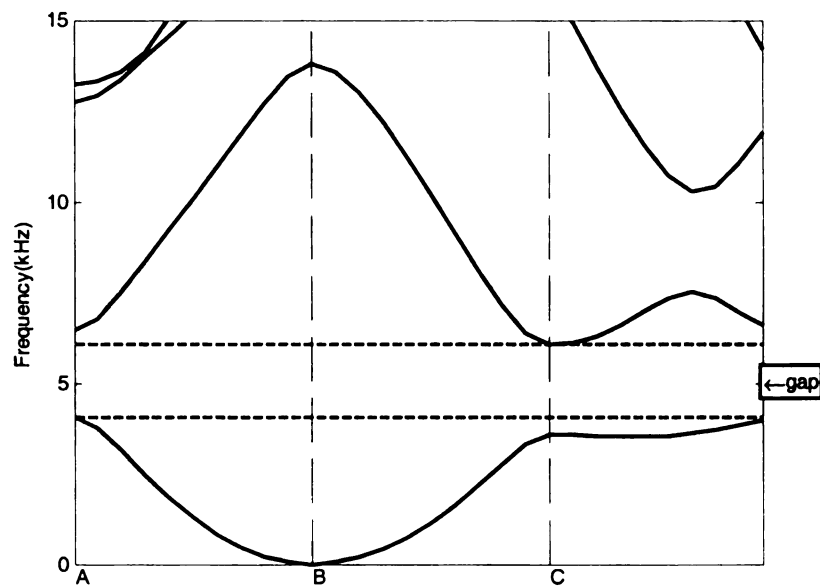
(b) Dispersion diagram

Figure 17. Mass distribution and dispersion diagram for design 10 in Table 2

(a) Optimal mass distribution graph

(b) Dispersion diagram

Figure 18. Mass distribution and dispersion diagram for design 11 in Table 2

(a) Optimal mass distribution graph

(b) Dispersion diagram

Figure 19. Mass distribution and dispersion diagram for design 12 in Table 2

(a) Optimal mass distribution graph

(b) Dispersion diagram

Figure 20. Mass distribution and dispersion diagram for design 13 in Table 2

(a) Optimal mass distribution graph

(b) Dispersion diagram

Figure 21. Mass distribution and dispersion diagram for design 14 in Table 2

(a) Optimal mass distribution graph

(b) Dispersion diagram

Figure 22. Mass distribution and dispersion diagram for design 15 in Table 2

5.1.3   Examples of Square Structures Using Formulation 2
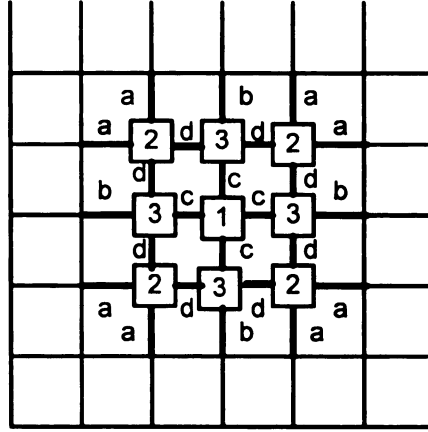
Figure 23. Locations of design masses and design elements in formulation 2

In this section, the square grid structure as in Section 5.1.1 is optimized using some of the bars as design variables (labeled a, b, c, and d in Figure 23), as well as the potential addition of non-structural masses (labeled 1, 2, and 3 in Figure 23). The constraints are chosen as follows:

$$x_{\max} = 0.5 m_{cell}$$

$\Lambda=9$ (no total allowable mass constraint)

$$r_{\min} = 0.5 r_0 \text{ and } r_{\max} = 2 r_0$$

where r_0 is the element radius of the homogeneous structure. The modified formulation (46), which studies the effect of changing the bar radii on the stiffness only, is used here to maximize band gaps above band 1 and band 3. The results are given in Table 3 and Figure 24 through Figure 29.

Table 3 shows that the gap above band 3 can be increased significantly by allowing more elements to be "designable". By having 2, 3, and 4 design elements, designs 17, 19, and 21 have band gaps above band 3 of 2.5 kHz, 4.0 kHz and 5.3 kHz respectively. Using

3 and 4 design elements in square cell, designs 19 and 21 are found to have the same

mass distribution as the result for design 14 of skew cell examples in Table 2, but design

14 has a gap of only 0.2 kHz.

However, increasing the number of design elements does not always help create

bigger gaps above band 1. For example, design 18 uses one more design element than

design 16, but both of the optimal designs have the same gap size of 1.2 kHz. In addition,

Design 18, which uses 3 design elements for square cell, places the same masses on the

cell as for design 10 of skew cell examples (Table 2), where no design elements are

allowed, but design 18 has a smaller gap of 1.2 kHz compared to a gap of 2.1 kHz for

design 10.

The rules of the mass distribution for formulation 1 discussed in Section 5.1.1 still hold

for formulation 2. In addition, the upper bounds and the lower bounds of the optimal gaps

above band 1 occur at the same positions (k vectors) as in the results for examples using

formulation 1.

Table 3. Local optima in examples of square structure using formulation 2 ($\alpha=90°$)

| Design No.	Optimal Design					Optimal Gap		
	$x^1 (\times m_{cell})$		$x^2 (\times r_0)$					
	$\{x_1, x_2, x_3\}$	Total Mass Used	a, b	c	d	Gap Size (kHz)	Abv Band	Abv Freq. (kHz)
16	0.50 0.00 0.50	2.50	1.30 2.00	**	**	1.2	1	3.4
17	0.02 0.20 0.50	2.82	0.50 0.50	**	**	2.5	3	5.3
18	0.50 0.00 0.19	1.26	1.36 2.00	0.50	**	1.2	1	3.8
19	0.00 0.50 0.50	4.00	0.50 0.50	2.00	**	4.0	3	4.4
20	0.50 0.00 0.21	1.34	1.28 2.00	0.80	0.50	1.4	1	3.3
21	0.00 0.50 0.50	4.00	0.92 0.50	2.00	2.00	5.3	3	7.9

** Not used as a design element
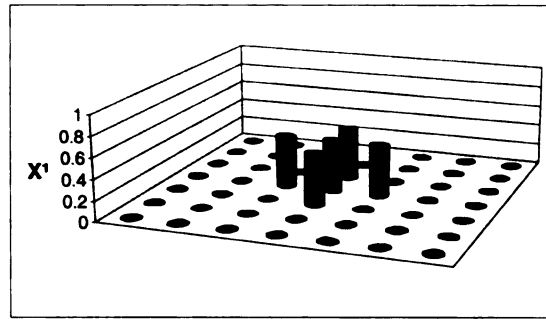
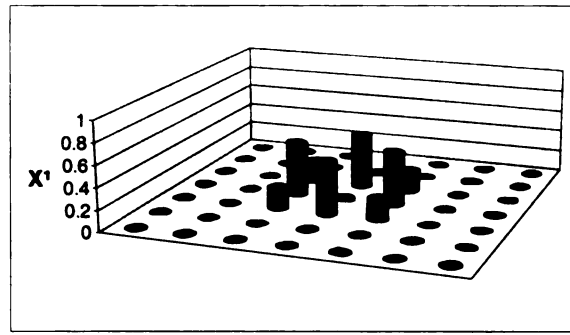(a) Optimal mass distribution graph
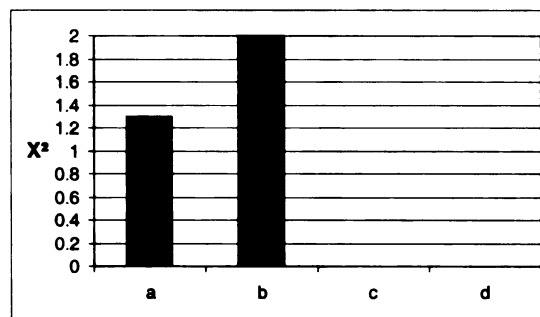
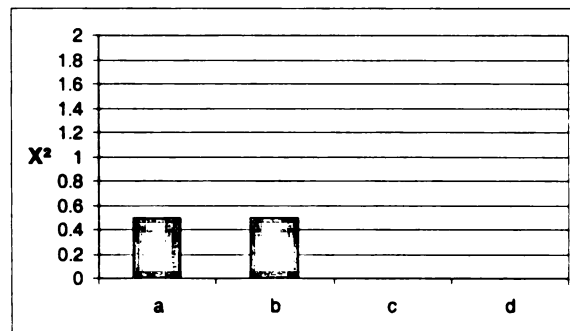(b) Optimal element radius graph
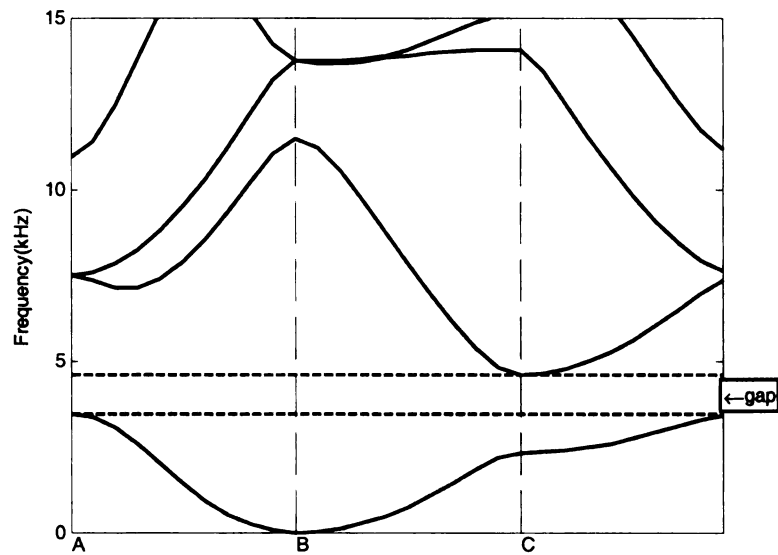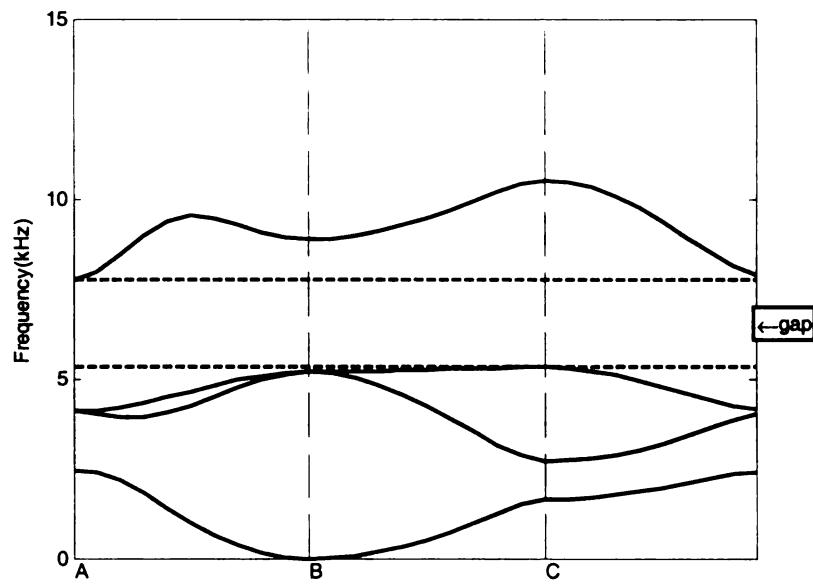

(c) Dispersion diagram

Figure 24. Mass and radius distribution and dispersion diagram for design 16 in Table 3

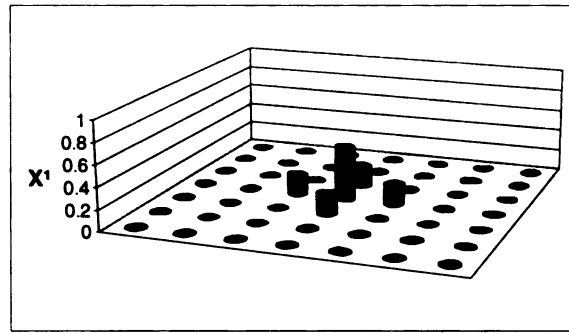(a) Optimal mass distribution graph
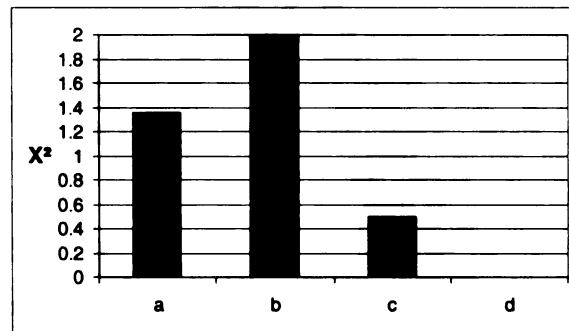

(b) Optimal element radius graph
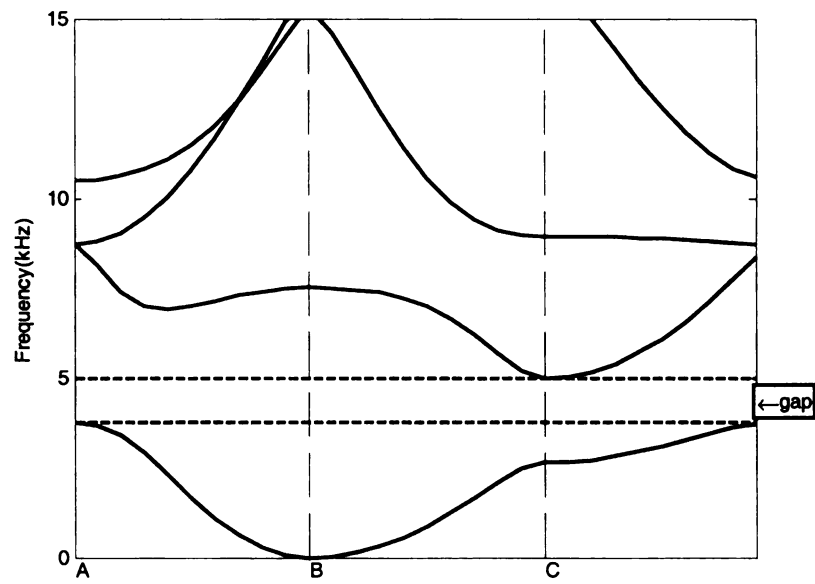

(c) Dispersion diagram

Figure 25. Mass and radius distribution and dispersion diagram for design 17 in Table 3
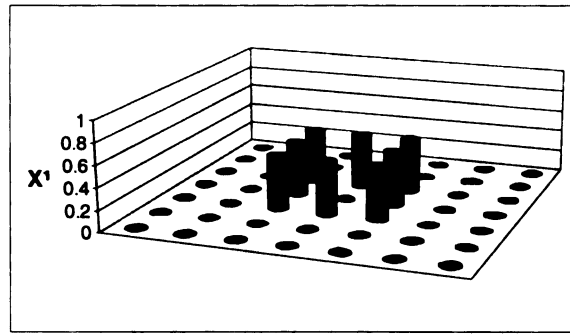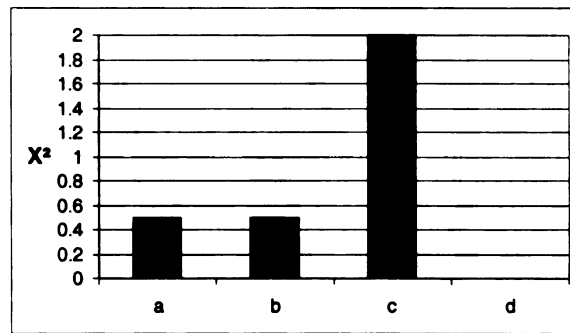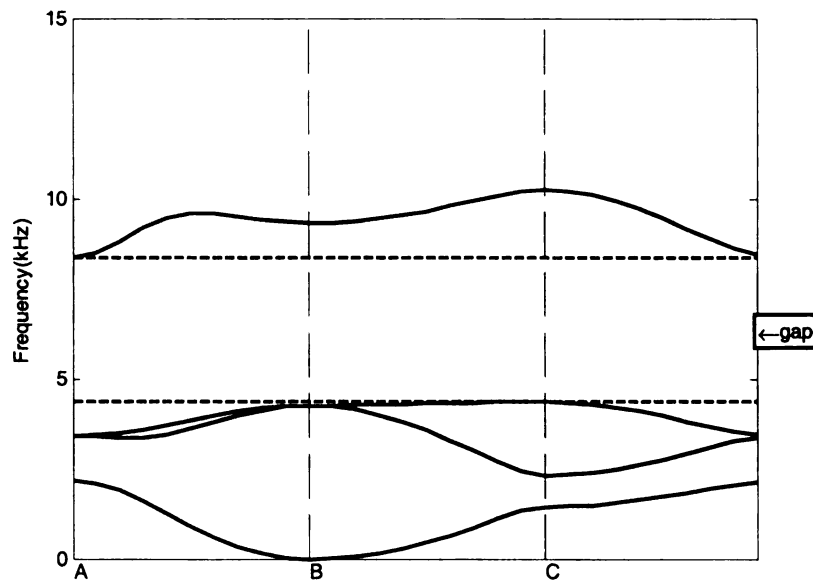
(a) Optimal mass distribution graph

(b) Optimal element radius graph

(c) Dispersion diagram

Figure 26. Mass and radius distribution and dispersion diagram for design 18 in Table 3

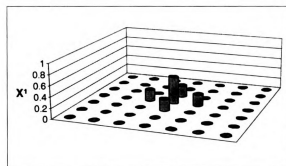(a) Optimal mass distribution graph

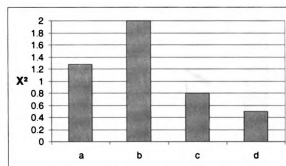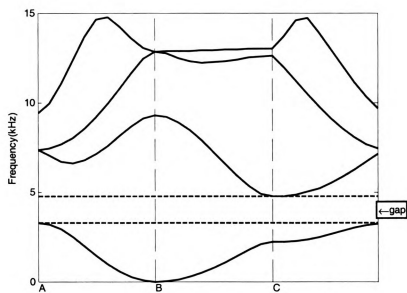(b) Optimal element radius graph

(c) Dispersion diagram

Figure 27. Mass and radius distribution and dispersion diagram for design 19 in Table 3
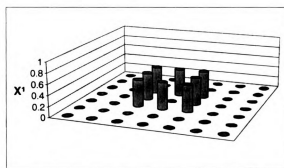
(a) Optimal mass distribution graph
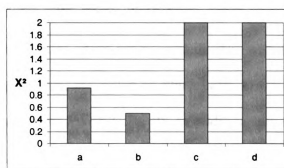

(b) Optimal element radius graph
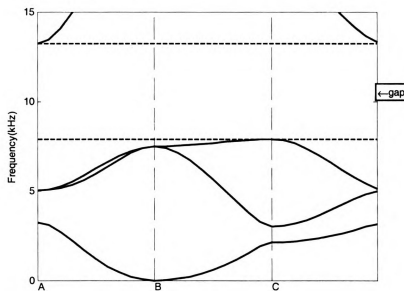

(c) Dispersion diagram

Figure 28. Mass and radius distribution and dispersion diagram for design 20 in Table 3

(a) Optimal mass distribution graph

(b) Optimal element radius graph

(c) Dispersion diagram

Figure 29. Mass and radius distribution and dispersion diagram for design 21 in Table 3

5.2 Discussion

The optimal solutions of all the examples in the last section demonstrate some common phenomena in terms of optimal mass distributions, and points k where the upper bounds and lower bounds of the optimal gaps are achieved. These phenomena are investigated further in the following sections.

### 5.2.1 Stationary Points on the Dispersion Diagram

On the dispersion diagrams of all the optimal designs with gaps above band 1, the lower bounds of the gaps occur at point A at which $k=(\pi, \pi)$ while the upper bounds are achieved at point C associated with $k=(\pi, 0)$. In addition, the eigenvalues at the gap bounds are distinct for all these examples. On the dispersion diagrams of the optimal designs with gaps above band 3, the upper bounds of the band gap are obtained at point A associated with $k=(\pi, \pi)$, but there are two cases for the lower bounds:

1. The lower bounds occur at point B associated with $k=(0,0)$ and at this point the eigenvalue is unique.

2. The lower bounds occur anywhere else and the eigenvalue of band 3 at point B associated with $k=(0,0)$ is repeated.

The above observations suggest that the critical points A, B, and C are stationary points on the dispersion diagram provided that the eigenvalues at these points are distinct. This is supported by the Propositions discussed in Section 3.7.1.These Propositions also show that the eigenvectors associated with the eigenvalues at these critical points are real. In the next section, we demonstrate that the optimal mass distribution is governed by these real eigenvectors.

5.2.2 Optimal Mass Distribution

The real eigenvectors associated with the distinct eigenvalues at the critical points A B and C represent standing waves or mode shapes that govern the optimal mass distribution. For example, both optimal results of design 5 in Table 1 and design 13 in Table 2 place the same amount of mass at location 1. The mode shapes in a representative cell depicted by the eigenvectors associated with the lower bounds and upper bounds of the optimal band gaps for these two designs are given in Figure 30 and Figure 31. The eigenvector components corresponding to out-of-plane translations are normalized so that the maximum component amplitude equals one. Interestingly, although one design is for square structure and the other one is for skew structure, the amplitude average of the eigenvector components corresponding to the out-of-plane translations of each potential additional mass location has the same profiles for both designs, as illustrated in Figure 32. Since location 1 has the maximum value of translation amplitude among the three potential mass locations (Figure 32 (a)) in the modes associated with the lower bounds of optimal gaps above band 1, adding mass to this spot reduces the lower bounds most efficiently. On the other hand, in the mode shapes associated with the upper bounds of optimal gaps above band 1, location 1 rests at the nodal point, which has zero translation (Figure 32 (b)). Adding mass to this point does not change the upper bounds.
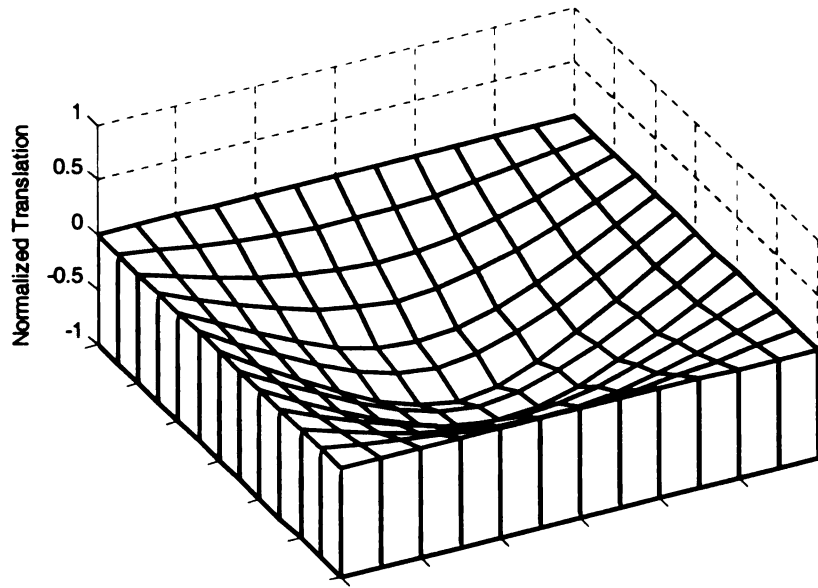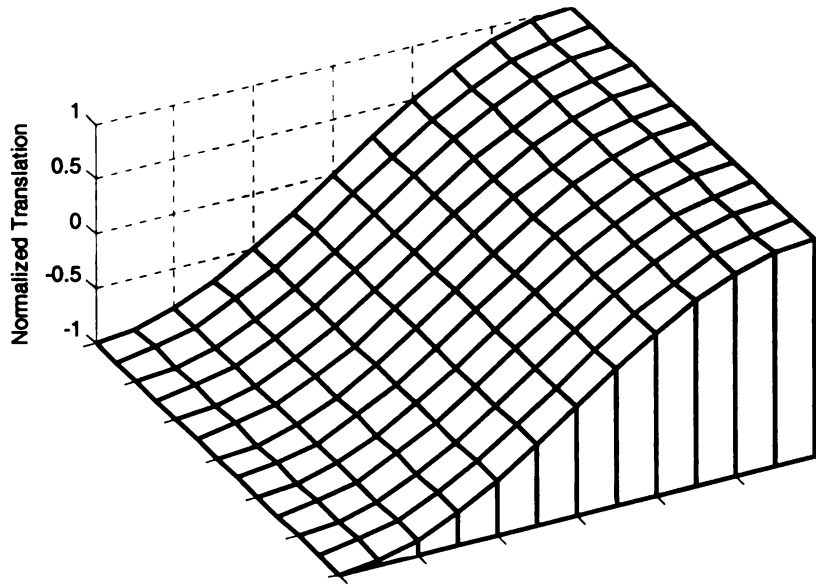
(a) Vibration mode of square cell(design 5 in Table 1)
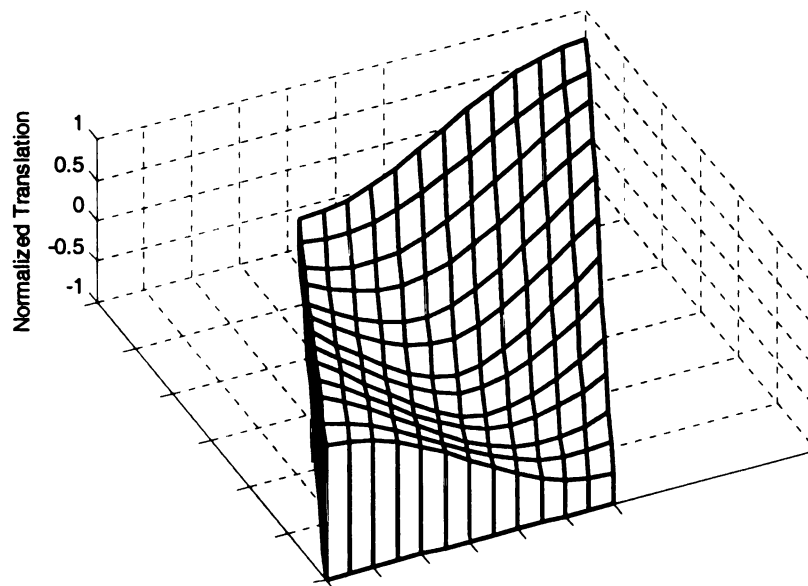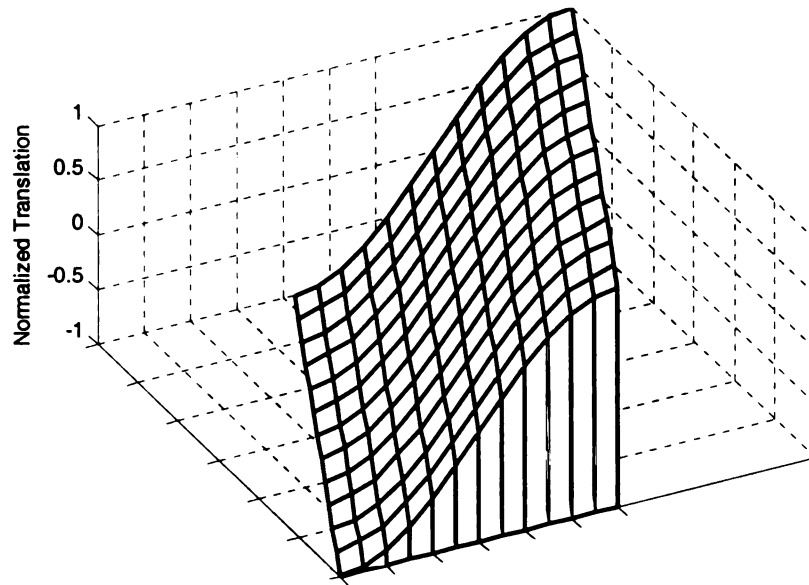

(b) Vibration mode of skew cell (design 13 in Table 2)

Figure 30. Vibration modes at lower bounds of optimal gaps above band 1
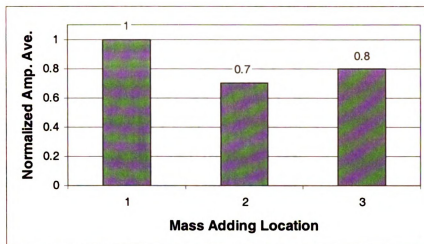
(a) Vibration mode of square cell(design 5 in Table 1)

(b) Vibration mode of skew cell (design 13 in Table 2.)
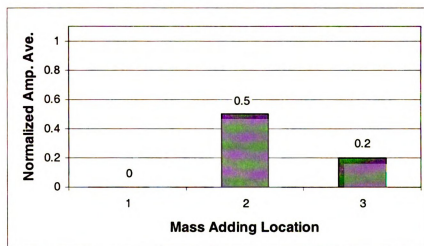
Figure 31. Vibration modes at upper bounds of optimal gaps above band 1
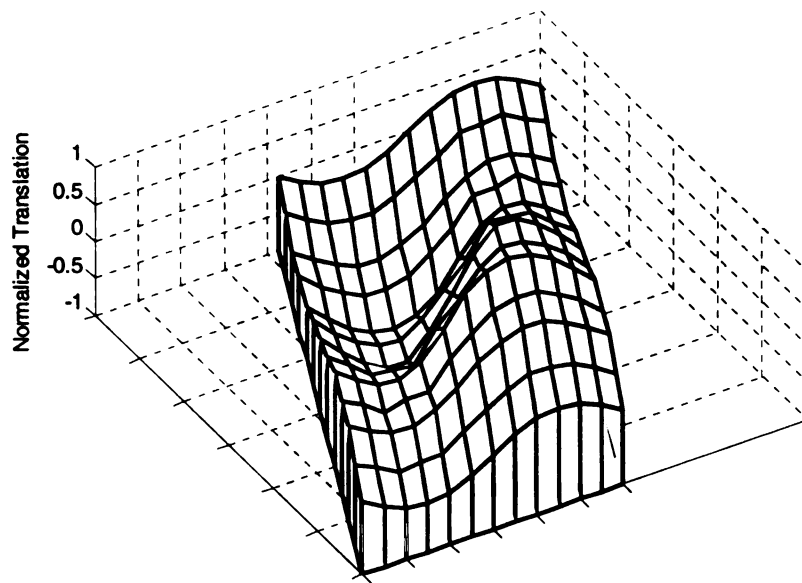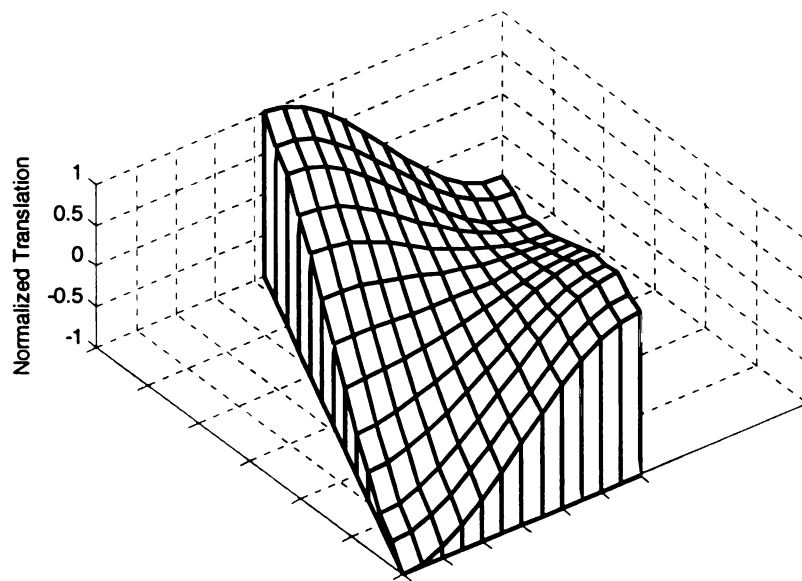
(a) For lower bound modes (Figure 30)

(b) For upper bound modes (Figure 31)

Figure 32. Eigenvector component profiles for modes in Figure 30 and Figure 31

(a) Vibration mode at lower bound

(b) Vibration mode at upper bound

Figure 33. Vibration modes at the bounds of optimal gap above band 3
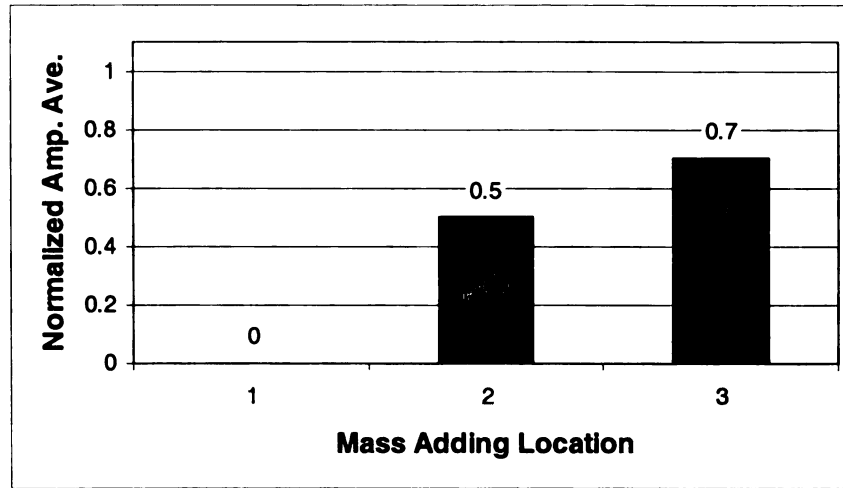
(a) For lower bound mode (Figure 33(a))
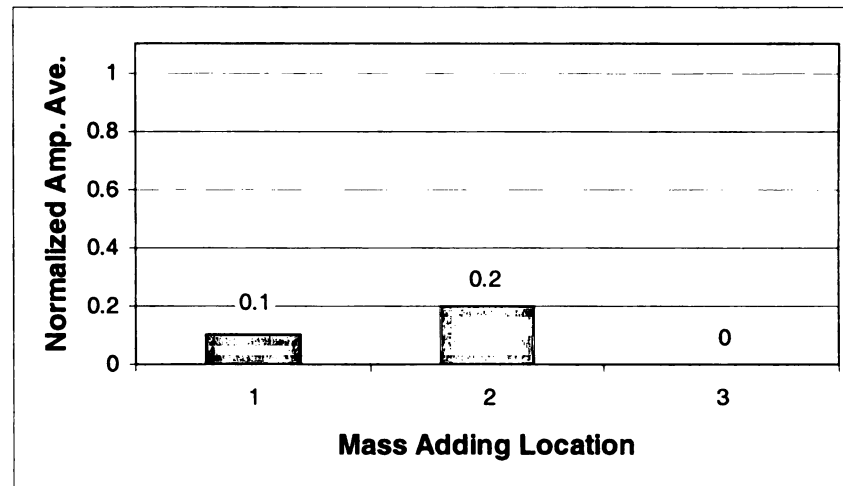
(b) For upper bound mode (Figure 33(b))

Figure 34. Eigenvector component profiles for modes in Figure 33

The above discussion explains why the mass placed at location 1 always reaches the

upper bound (x_{max}) in the examples maximizing gap above band 1. By the same

principle, the optimal mass distribution for design 15 in Table 2, where a gap is sought

above band 3, can be explained easily. The vibration modes associated with the lower and

upper bounds of the gaps for this design are given in Figure 33 and the profiles of the

amplitude average of the eigenvector components corresponding to the out-of-plane

translations of each potential additional mass location are given in Figure 34.

Chapter 6 Wave Propagation in Finite 2D Grid Structures

Wave propagation in infinite periodic plane grid structures was studied in Chapters 4-5. In this chapter the behavior of finite periodic plane grid structures subjected to harmonic loading perpendicular to the grid plane is investigated considering two applications: filters and wave guides.

In order to reduce computer memory requirements for computing the response of finite periodic plane grids, finite plane grids made of 2x2 square cells (Figure 35 (a)) and 2x2 skew cells (Figure 35 (b)) are considered here. The geometry of the grid element and material properties of the homogeneous structures used here are the same as in Section 5.1. Using optimization problem formulation 1 with one nonstructural mass adding location (labeled 1 in Figure 35), and setting $x_{max} = 1m_{cell}$ and $\Lambda=1$, the optimal solutions for maximizing gap above band 1 in infinite grids are found having one mass of x_{max} placed at the center of the cells and the dispersion diagrams are given in Figure 36.

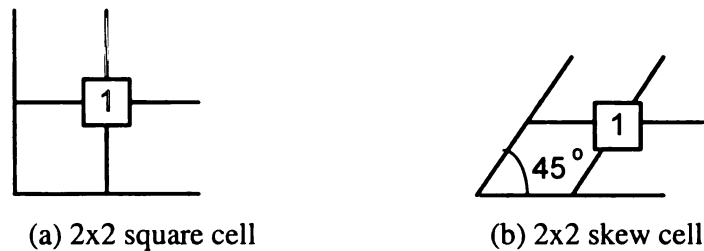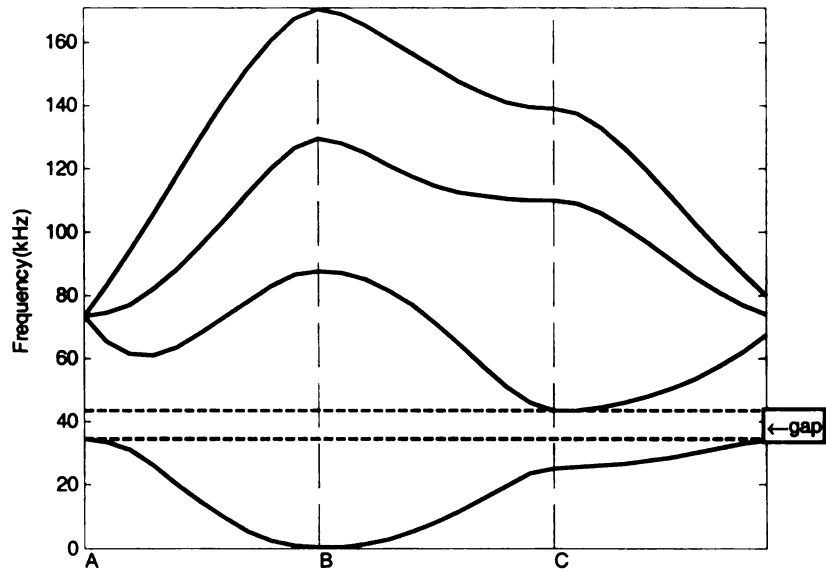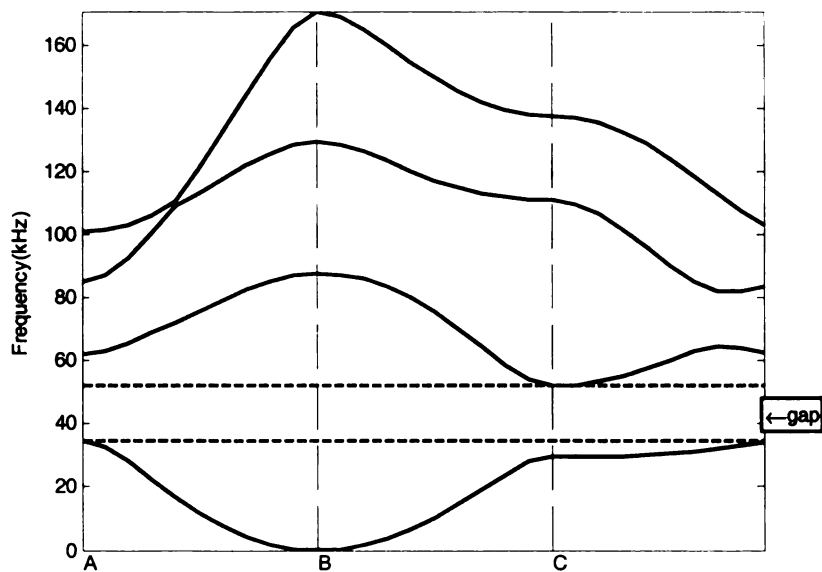(a) 2x2 square cell   (b) 2x2 skew cell

Figure 35. 2x2 representative cells for finite 2D grids

(a) Structure made of 2x2 square cell; Gap is 9.0 kHz above 34.6 kHz

(b) Structure made of 2x2 skew cell; Gap is 17.5 kHz above 34.5 kHz

Figure 36. Dispersion diagrams for infinite optimal structures made of 2x2 cells

6.1 Model Equations

In Chapter 3, the FE expression of equations of motion for infinite 2D periodic grid is derived using Bloch-Floquet theorem and the representative cell. To derive the equations of motion for finite 2D grid, the whole structure must be treated using the FE method. Let $u \in C^{TOT}$, $\overline{M} \in \Re(TOT,TOT)$ and $\overline{K} \in \Re(TOT,TOT)$ denote the displacement vector, and assembled mass and stiffness matrices, where TOT is the total number of degrees of freedom in the whole finite structure. Let $fe^{i\omega t}$ represent the periodic loading vector, where $f \in \Re^{TOT}$ is a vector of force amplitudes and ω is the driving frequency. The equations of motion for finite 2D grid then take the form of (24) as

$$\overline{M}\ddot{u} + \overline{K}u = fe^{i\omega t} \tag{67}$$

Upon substitution of $u = ae^{i\omega t}$ (recall from (25) that a is the wave amplitude vector), the above equation yields

$$(\overline{K} - \omega^2\overline{M})a = f \tag{68}$$

For a given finite periodic structure and harmonic loading, a can be obtained using (68). The behavior of the finite periodic plane grid structure is then studied using the relative components of a.

6.2 Examples

Periodic plane grids can be used to generate vibration filters and wave guides. The 2x2 representative cells in Figure 35 are used here to demonstrate the applications of finite 2D grids. The finite periodic grid structures acting as filters and wave guides are constructed by continuously putting *NC1* and *NC2* representative cells along tiling

vectors $t^{(1)}$ and $t^{(2)}$ respectively, where *NC1* and *NC2* represent the total cell numbers along tiling vectors $t^{(1)}$ and $t^{(2)}$ in the finite structures.

6.2.1 Filters

In the examples for filter application, a harmonic force perpendicular to the plane of grid structures is applied at each node of the periodic structure, and the force amplitude is kept constant while the driving frequency varies from zero to a value above the upper bound frequency of the optimal gaps in infinite structures. All the nodes on the four edges of the structures are pinned. The translation amplitudes of the nodes in the 4 cell ×4 cell area located at the center of the structures are computed for each driving frequency. The harmonic loading and the response evaluation area in the finite periodic square structures used as filters are illustrated in Figure 37.

Let χ denote the set of the nodes where the responses are evaluated and $a_n(\omega)$ represent the translation amplitude of node $n \in \chi$ at driving frequency ω. The frequency response function (FRF) is then calculated using the following formula:

$$\text{FRF} = 20\log(\max_{n \in \chi}(\frac{a_n(\omega)}{a_n(\omega = 0)}))$$ (69)

Figure 38 displays the FRF curves for the square and skew periodic structures with *NC1=NC2=*6, 10 and 16. For comparison, the bounds of band gaps for infinite structures are shown using vertical dashed lines. The band gaps are observed for all the cases in both square and skew structures and with more cells used in the finite structures, the gaps get closer to the gaps in the infinite structures. However, resonance peaks are noted just above the lower bound of the gap for square structures, and at 37.1 kHz, which is 2.6 kHz

above the lower bound of the gap for skew structures. With the increase of the number of the cells included in the finite structures, the peaks get lower.
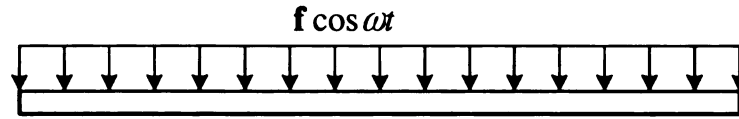
(a) Harmonic loading perpendicular to the grid plane
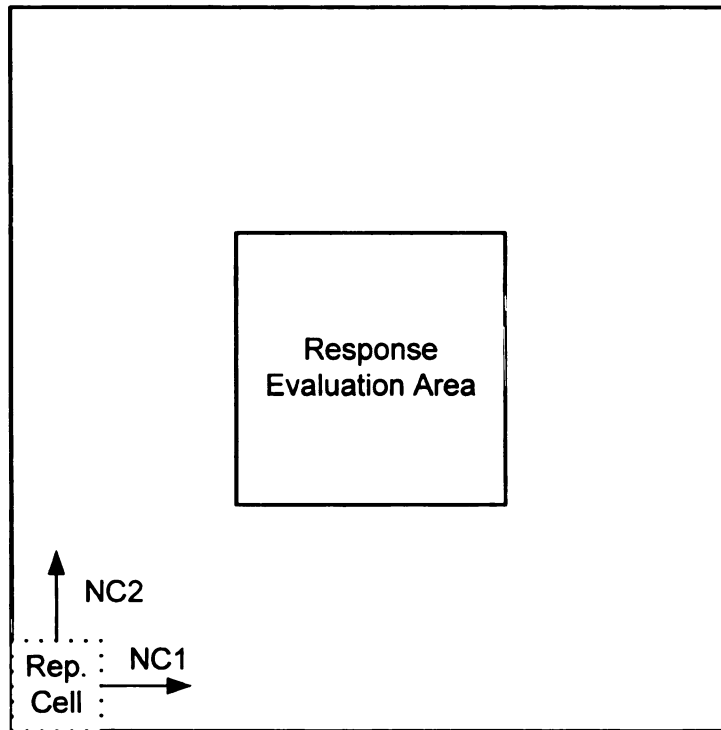
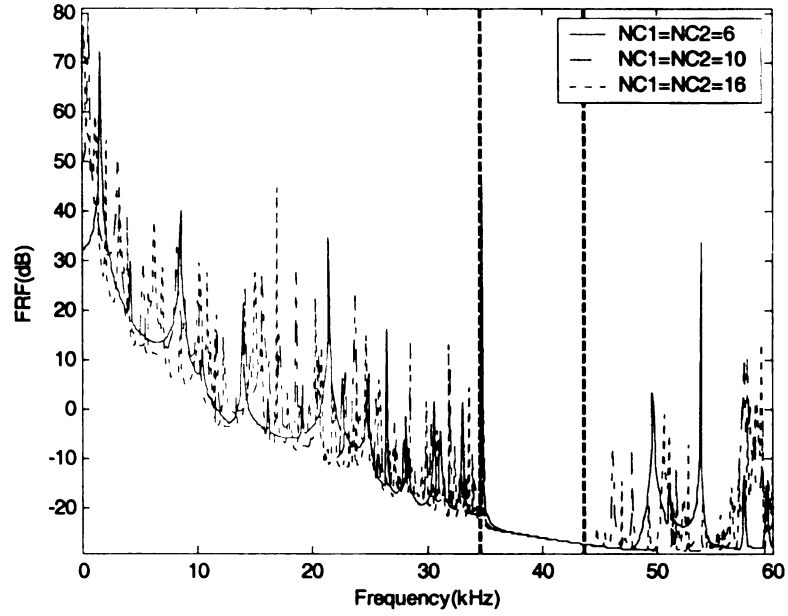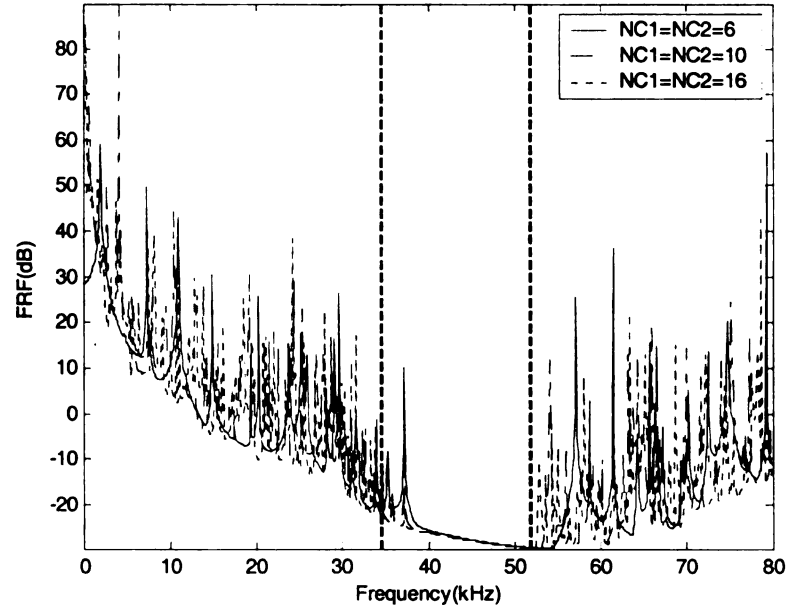

(b) Layout of structure construction and response evaluation area

Figure 37. Finite filter structure subjected to harmonic loading

(a) Response of square filter structure

(b) Response of skew filter structure

Figure 38. Response of filter structures with *NC1* × *NC2* Cells

6.2.2 Wave Guides

In this section, a defect is introduced into finite periodic structures by removing the nonstructural masses from the cells in a path from a point excitation to a response evaluation point. Figure 39 illustrates the loading point F and response evaluation points A and B for finite structures made of square 2x2 cells (Figure 35 (a)) with $NC1=NC2=16$. The boundary conditions are the same as in last section. A point harmonic driving force $f\cos\omega t$ is applied at the node (point F). The nonstructural masses are removed from the cells in a bent path from point F to point B along the tiling vectors $\mathbf{t}^{(1)}$ and $\mathbf{t}^{(2)}$ of square structures. In this case, the FRF is calculated using the following formula:

$$FRF = 20\log(\frac{a_{A/B}(\omega)}{a_{A/B}(\omega=0)}) \tag{70}$$

where $a_{A/B}(\omega)$ represents the translation amplitude of node A or B depending on which point where the response is evaluated. Figure 40 (a) shows the FRF curves for points A and B. It can be seen that the response at point A, between which and the excitation point F perfect periodic cells with nonstructural masses are used, drops significantly in the band gap range, whereas the response at point B remains high indicating the harmonic excitation transmitted through the bent path made of homogeneous cells.

With the 2x2 square cells in Figure 39 replaced by 2x2 skew cells (Figure 35 (b)), the responses at point A and B for the skew structure are shown in Figure 40 (b).
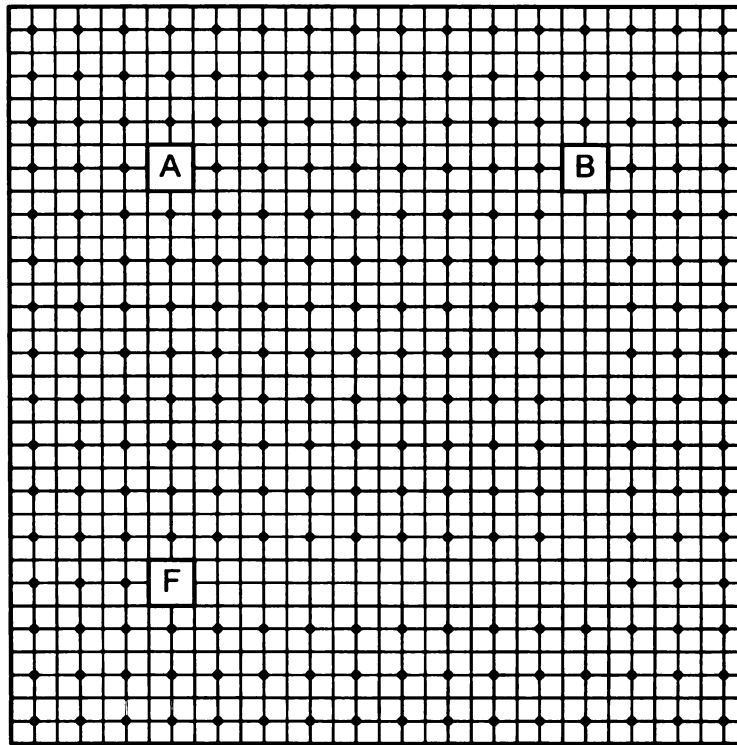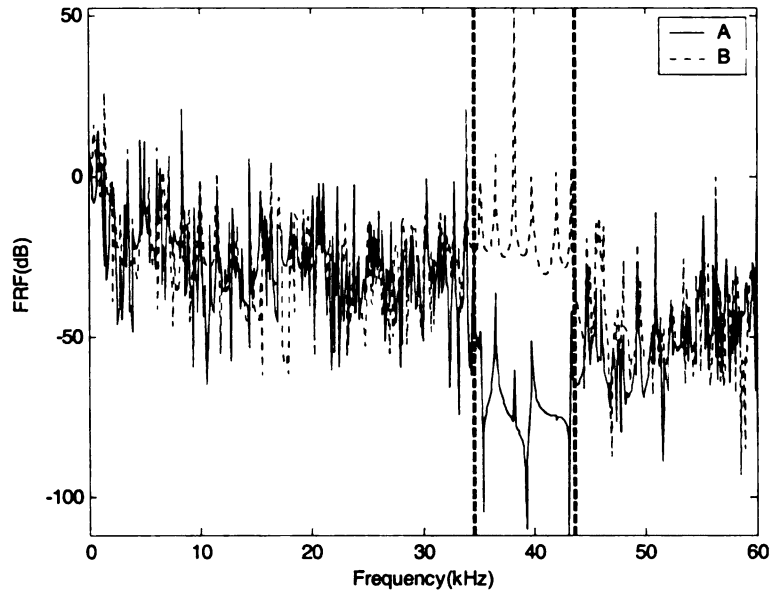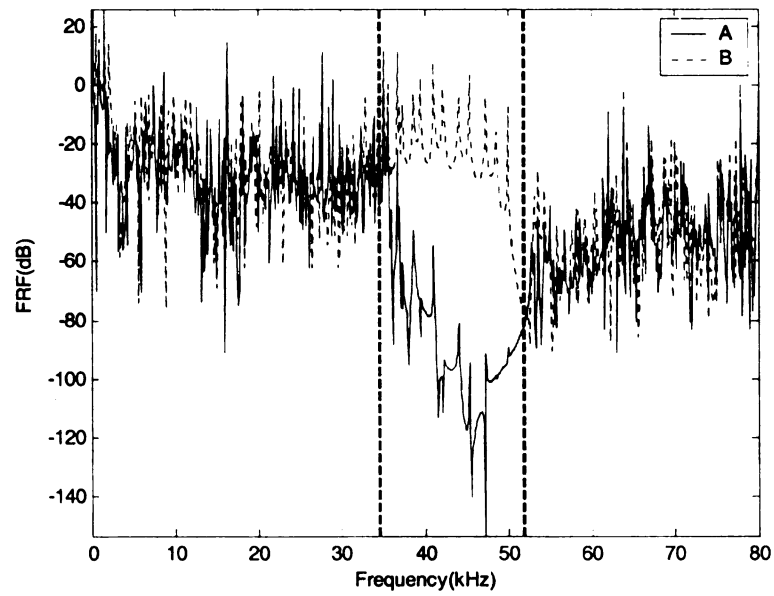
Figure 39. Layout of loading and response evaluation locations for wave guide structures

(a) Response of square wave guide structure

(b) Response of skew wave guide structure

Figure 40. Response of wave guide structures

Chapter 7 Conclusions

7.1 Summary

A method using an FE model, Bloch-Floquet theory and optimization technique has been presented for designing infinite periodic plane grid structures with frequency band gaps. This method is implemented numerically using two different periodic structures, a square structure and a skewed one, and two different optimization formulations. In one formulation the selective addition of lumped masses is used to optimize the structures and in the other formulation the stiffness of the grid structure is also allowed to change in addition to the selective addition of lumped masses. The numerical results for infinite periodic structures can be summarized as follows:

1. The optimal mass distribution is related to the eigenvectors associated with the bounds of the optimal gaps.

2. The bounds of optimal gaps on the dispersion diagrams tend to occur at the critical points associated with k=(π, π), (0, 0) and (π, 0). Analysis shows that when differentiability can be ascertained, these critical points are stationary points on the dispersion diagram and therefore potential candidate solutions to the minimum and maximum problems in (31).

3. Given the same design constraints, skew structures are more advantageous than square structures to create bigger gaps above lower bands such as band 1 and band 3.

4. By allowing more grid elements to be "designable" in a square structure, the gap above mode 3 can be increased significantly.

Wave propagation in finite periodic plane grid structures is investigated by considering the response of finite periodic plane grid structures subjected to harmonic loading using two applications: filter and wave guide. The numerical results for finite periodic structures show the following:

1. The response of perfect finite periodic structures is attenuated significantly within the frequency ranges of the band gaps for the corresponding infinite periodic structures. With more cells included in the finite periodic structures, the band gap range exhibited in the finite periodic structures gets closer to that in the corresponding infinite ones.

2. A wave can propagate through a wave guide path in finite periodic structures without attenuation when a defect is introduced to the structures by removing the nonstructural mass in the cells along the wave guide path.

7.2   Areas of Future Work

Based on the conclusions, the following areas should be explored:

1. The optimization problem is inherently non-smooth and the loss of differentiability is always a strong possibility. The problem may have many local solutions and is difficult to solve using standard mathematical programming tools. Further work could focus on developing enhanced algorithms specially tailored for this application.

2. The geometry of the structure has a large effect on the optimal gaps in the structure. In a different formulation, the angle α between the two tiling vectors may be considered as a design variable.

3. The gap information obtained by studying infinite periodic structures can provide a good prediction of the gap in finite periodic structures. However, to make a vibration filter or a wave guide for engineering applications, the effect of boundary conditions, damping, and imperfections on the band gaps in finite structures should be studied.

BIBLIOGRAPHY

[1].   L. Brillouin, *Wave propagation in periodic structure*, 2nd edition, Dover, New York, 1953.

[2].   D. J. Mead, Wave Propagation in continuous periodic structures: research contributions from Southhampton 1964-1995, *Journal of Sound and Vibration* 190 (1996) 495-524.

[3].   J. P. Dowling, H. Everitt and E. Yablonovitch, photonic and sonic band-gap bibliography, http://home.earthlink.net/~jpdowling/pbgbib.html, 2001.

[4].   P. G. Martinsson and A. B. Movchan, Vibrations of lattice structures and phononic band gaps, *Q. Jl Mech. Appl. Math.* 56 (2003) 45-64.

[5].   J. S. Jensen, Phononic band gaps and vibrations in one- and two-dimensional mass-spring structures, *Journal of Sound and Vibration* 266 (2003) 1053-1078.

[6].   O. Sigmund, Microstructural design of elastic band gap structures, *Proceedings of the Second World Congress of Structural and Multidisciplinary Optimization*, Dalian, China, 2001.

[7].   O. Sigmund and J. S. Jensen, Topology optimization of phononic band gap materials and structures, *Fifth World Congress on Computational Mechanics.*, Vienna, Austria, 2002.

[8].   O. Sigmund and J. S. Jensen, Systematic design of phononic band gap materials and structures by topology optimization, *Phil. Trans. R. Soc. Lond.* A 361 (2003) 1001-1019.

[9].   S. J. Cox and D. C. Dobson, Maximizing band gaps in two-dimentional photonic crystals, *SIAM J. Appl. Math.* 59 (1999) 2108-2120.

[10]. S. J. Cox and D. C. Dobson, Band structure optimization of two-dimensional photonic crystals in H-polarization, *Journal of Computational Physics* 158 (2000) 214-224.

[11]. S. Parmley, T. Zobrist, T. Clough, A. Perez-miller, M. Makela and R. Yu, Phononic band structure in a mass chain, *Applied Physics Letters* 67 (1995) 777-779.

[12]. M. Kafesaki, M. M. Sigalas and E. N. Economou, Elastic wave band gaps in 3-D periodic polymer matrix composites, *Solid State Communications* 96 (1995) 285-289.

[13]. J. O. Vasseur, P. A. Deymier, G. Frantziskonis, G. Hong, B. Djafari-rouhani and L. Dobrzynski, Experimental evidence for the existence of absolute acoustic band gaps in two-dimensional periodic composite media, *Journal of Physics: Condensed Matter* 10 (1998) 6051-6064.

[14]. M. M. Sigalas and E. N. Economou, Elastic waves in plates with periodically placed inclusions, *Journal of Applied Physics* 75 (1994) 2845-2850.

[15]. M. Heckel, Investigations on the vibrations of grillages and other simple beam structures, *Journal of the Acoustical Society of America* 36 (1964) 1335-1343.

[16]. R. M. Orris and M. Petyt, A finite element study of harmonic wave propagation in periodic structures, *Journal of Sound and Vibration* 33 (1974) 223-236.

[17]. P. Langlet, A.-C. Hladky-Hennion and J.N. Decarpigny, Analysis of the propagation of plane acoustic waves in passive periodic materials using the finite element method, *Journal of the Acoustical Society of America* 98 (1995) 2792-2800.

[18]. C. Kittel, *Introduction to Solid State Physics*, 7th edition, Wiley, New York, 1996.

[19]. K. Svanberg, The method of moving asymptotes, *Int. J. Num. Mech. Eng.* 24 (1987) 359-373.